

DMESA: Densely Matching Everything by Segmenting Anything

Yesheng Zhang, Xu Zhao, *Member, IEEE*

Abstract—We propose MESA and DMESA as novel feature matching methods, which utilize *Segment Anything Model* (SAM) to effectively mitigate matching redundancy. The key insight of our methods is to establish implicit-semantic *area matching* prior to point matching, based on advanced image understanding of SAM. Then, informative area matches with consistent internal semantic are able to undergo dense feature comparison, facilitating precise inside-area point matching. Specifically, MESA adopts a sparse matching framework and first obtains candidate areas from SAM results through a novel Area Graph (AG). Then, area matching among the candidates is formulated as graph energy minimization and solved by graphical models derived from AG. To address the efficiency issue of MESA, we further propose DMESA as its dense counterpart, applying a dense matching framework. After candidate areas are identified by AG, DMESA establishes area matches through generating dense matching distributions. The distributions are produced from off-the-shelf patch matching utilizing the Gaussian Mixture Model and refined via the Expectation Maximization. With less repetitive computation, DMESA showcases a speed improvement of nearly five times compared to MESA, while maintaining competitive accuracy. Our methods are extensively evaluated on five datasets encompassing indoor and outdoor scenes. The results illustrate consistent performance improvements from our methods for five distinct point matching baselines across all datasets. Furthermore, our methods exhibit promise generalization and improved robustness against image resolution variations. The code is publicly available at github.com/Easonyesheng/A2PM-MESA.

Index Terms—Feature Matching, Area Matching, Segment Anything Model.

arXiv:2408.00279v1 [cs.CV] 1 Aug 2024

1 INTRODUCTION

FEATURE matching aims at establishing correspondences between images, which is vital in a broad range of applications, such as SLAM [1], SfM [2] and visual localization [3]. However, achieving exact point matches is still a challenge due to the presence of matching noises [4], including scale variations, viewpoint and illumination changes, repetitive patterns, and poor texturing.

Recent years have witnessed significant advancements in learning-based feature matching. Classical sparse matching methods have been revolutionized by learning detectors [5], [6], descriptors [7], [8] and matchers [9], [10]. Meanwhile, learning-based semi-dense [11], [12] and dense [13] methods further obtain an impressive precision gap over their sparse counterparts, by dense feature comparison across entire images. Nevertheless, all these matching methods encounter a common obstacle: **matching redundancy**. In essence, the interaction of learning-based features in irrelevant image regions is prone to the matching noises, thereby diminishing the matching performance of these methods.

Intuitively, most of the matching redundancy can be effectively identified through high-level image understanding, and only strongly correlated local **areas** (or **regions**) need dense feature comparison to determine precise matches (cf. Fig. 1). Therefore, recent methods [15], [16] perform learning-based overlap segmentation before matching. However, implicit learning needs non-reusable computational overhead and the redundancy persists in the overlap during detailed matching. To address these issues, some work turn to explicit semantic prior [17], [18]. Unlike manually specifying a topic number to group feature patches [17], *Area to Point Matching* (A2PM) framework proposed by SGAM [18] provides a more intuitive way to reduce matching redundancy. Specifically, this framework establishes semantic area matches

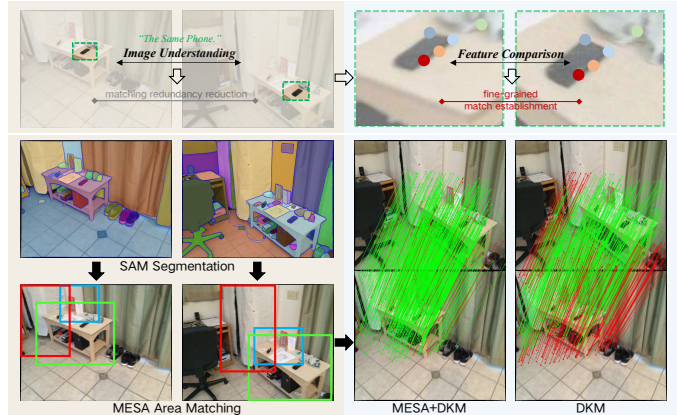


Fig. 1. **The matching redundancy reduction of our methods.** High-level image understanding enables efficient matching redundancy reduction, allowing for precise point matching by local dense feature comparison. Therefore, the proposed MESA effectively reduces the matching redundancy by area matching based on SAM [14] segmentation, significantly improving the accuracy of DKM [13].

first where matching redundancy is largely removed based on semantic, and then obtains accurate correspondences by point matching within these areas. Nevertheless, SGAM relies on semantic segmentation to guide area matches. Its performance, thus, decreases when encountering inexact semantic labeling and semantic ambiguity [18]. Furthermore, the benefits of A2PM cannot be extrapolated to more general scenes due to the close-set semantic labels. Hence, reducing matching redundancy through semantic segmentation suffers from impracticality.

Recently, Segment Anything Model (SAM) [14] has gained notable attention from the research community due to its exceptional performance and versatility, which can be the basic

The authors are with Department of Automation, Shanghai Jiao Tong University. E-mail: {preacher, zhaoxu}@sjtu.edu.cn
Corresponding author: Xu Zhao

front-end of different tasks [19], [20]. This suggests that the foundation model can accurately comprehend image contents across various domains. Drawing inspiration from this, we realize that the image understanding of SAM can be leveraged to reduce matching redundancy. Thus, we propose to establish area matches based on SAM segmentation to overcome limitations of SGAM [18]. Similar to the semantic segmentation, the image segmentation also provides multiple areas in images, but without semantic labels attached to these areas. However, the general object perception of SAM ensures that its segmentation results inherently contain implicit semantic information. In other words, a complete semantic entity is always segmented as an independent area by SAM. Hence, matching these *implicit* semantic areas also effectively reduces matching redundancy and promotes accurate point matching within areas [18]. Furthermore, the absence of explicit semantics alleviate issues of inaccurate area matching caused by erroneous labeling. The limitation of generalization due to semantic granularity is also overcome. Nevertheless, area matching can not be simply achieved by semantic labels but requires other approaches under this situation.

In this work, we propose Matching Everything by Segmenting Anything (MESA, Fig. 3), a method for precise area matching from SAM segmentation. MESA focuses on **two main aspects**: *area relation modeling* and *area matching based on the relation*. In particular, since SAM areas only provide local information, matching them independently can lead to inaccurate results, especially in scenes with scale variation and repetitiveness. To address this, we construct a novel graph structure, named *Area Graph* (AG), to model the global context of areas as a basis for subsequent precise matching. AG takes areas as nodes and connects them with two types of edges: undirected edges for adjacency and directed edges for inclusion. Both edges capture global information, and the latter enables the construction of hierarchy structures similar to [21] for efficient matching. Based on the *relation modeling*, MESA performs area matching by deriving two graphical models from AG: *Area Markov Random Field* (AMRF) and *Area Bayesian Network* (ABN). The AMRF involves all global-informative edges, thus allowing global-consistent area matching through energy minimization on the graph. Specifically, the graph energy is determined based on the learning similarity and spatial relation between areas, making this energy minimization effectively solvable through the *Graph Cut* [22]. The ABN, furthermore, is proposed to facilitate the graph energy calculation, leveraging the hierarchy structure of AG. Finally, we propose a global matching energy to address the issue of multiple solutions in *Graph Cut*, ultimately leading to effective matching redundancy reduction.

Although MESA holds promise for high accuracy, its intricate process significantly diminishes its efficiency. To probe the root of this efficiency issue, we deeply review the matching procedure of MESA. Similar to the *sparse* framework in point matching, MESA essentially operates as a *sparse* area matching framework. It starts by extracting area candidates from images and subsequently conducts dense similarity computations between the candidate sets from the image pair. The considerable number of candidate areas leads to substantial computational overhead. Additionally, unlike points, determining similarities between areas is notably more expensive. Consequently, the efficiency drawback of MESA predominantly emerges from the costly computation of area similarities in the *sparse* matching framework.

To address this issue, we take inspiration from the dense framework employed in point matching [11], [13] and proposed

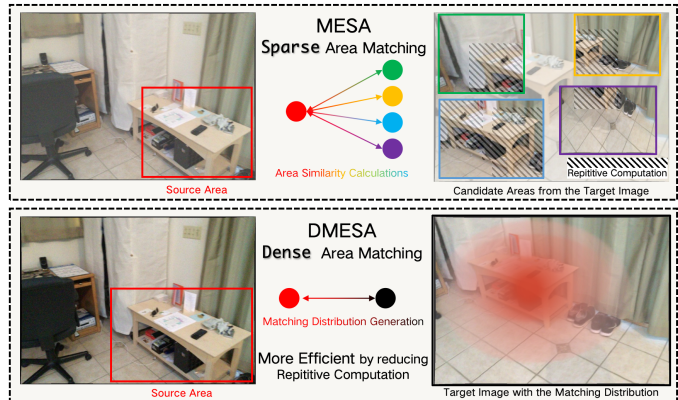


Fig. 2. **MESA vs. DMESA.** The sparse area matching framework of MESA involves repetitive computation in area similarity calculations, leading to an efficiency issue of MESA. To address this issue, DMESA leverages a dense matching distribution to guide the area matching, reducing repetitive computation.

a *Dense* version of MESA, named *DMESA*, to conduct a dense area matching framework. In contrast to common beliefs in point matching, a dense area matching framework is more efficient than a sparse one. This difference arises from the overlaps between basic units. In point matching, there are no overlaps among basic units (*i.e.* points). Thus, a dense framework that find correspondences from the entire image incurs significantly higher computational costs than a sparse framework that only considers keypoints. However, in area matching, the basic units (*i.e.* candidate areas) exhibit considerable overlap and often encompass the entire image (cf. Fig. 2 top). Thus, repetitive computations exist in the area similarities calculation of the sparse framework. Conversely, in a dense framework, these repetitive computations can be avoided by directly generating dense matching distributions on the entire image. Furthermore, we notice that these matching distributions can be derived through patch matching, mirroring the coarse matching stage of a current semi-dense point matcher [12].

Consequently, DMESA focuses on utilizing patch matching to achieve area matching (cf. Fig. 6). Specifically, it first establishes patch matches between a source area and the target image, leveraging the *off-the-shelf* coarse matching [12]. Then, it models the joint matching distribution of these patch matches using the Gaussian Mixture Model (GMM), which can be used to guide the following area matching. Considering the accuracy concerns of patch matching, DMESA introduces cycle consistency [23] to optimize the distribution, based on a finite-step Expectation Maximization (EM) algorithm. Afterwards, precise area matching can be obtained from the refined distribution.

This work is a extension version of MESA [24] presented at CVPR'24. Here, we introduce the following technical enhancements and experimental contributions: **1)** After delving into the efficiency issue of MESA, we propose its *dense* counterpart, named DMESA, applying a *dense area matching framework*. DMESA enables area matching derived from patch matching without additional training. In experiments, it can establish area matches with competitive accuracy at a speed nearly 5 times faster than MESA, offering a better precision/efficiency trade-off; **2)** We observe a substantial impact from image resolution on feature matching in experiments. Thus, we conduct an in-depth analysis of this impact, resulting in a improved configuration of A2PM. Moreover, we thoroughly examine image resolution in experiments, providing a more comprehensive evaluation of our methods; **3)** We add a

sparse point matching baseline in the experiments, to prove our methods can benefit all existing types of point matchers. By employing a more reproducible experimental setup, we present new results for previous experiments and conduct experiments on two additional indoor and outdoor datasets. Furthermore, experiments investigating cross-domain generalization and impact of model fine-tuning are conducted in this version.

Our work makes several contributions. **1)** We propose leveraging the high-level image comprehension capability of SAM to effectively reduce redundancy in feature matching. To this end, we devise two methods, *i.e.* *MESA* and *DMESA*, for area matching from SAM segmentation results and ultimately enhancing feature matching performance. **2)** Applying the sparse matching framework, *MESA* first extracts candidate areas from images by a novel graph, named AG, which models the global area relations. Then, precise area matching is achieved by *MESA*, based on graphical models derived from AG. **3)** To improve the efficiency of *MESA*, we further introduce *DMESA*, utilizing a dense framework to provide a better balance between accuracy and efficiency. *DMESA* achieves area matching by generating dense matching distributions on the entire image. These distributions are obtained from off-the-shelf patch matches, which are modeled by the GMM and refined by a finite-step EM algorithm. **4)** In extensive experiments on five diverse datasets, our methods yield substantial performance improvements for various point matchers across sparse, semi-dense, and dense matching frameworks. Moreover, our methods exhibit prominent cross-domain generalization and superior robustness against input image resolution, underscoring their practical utility.

2 RELATED WORK

2.1 Sparse, Semi-Dense and Dense Matching.

There are three types of feature matching methods: sparse, semi-dense and dense. Classical feature matching methods [25], [26] belongs to the sparse framework, which involves keypoint detection and description in images and matching among keypoint sets. The learning counterpart of this framework utilizes neural networks to perform feature detection [5], [27], description [7], [8], [28] or matching [9], [29]. To avoid the detection failure in sparse methods, semi-dense methods [11], [30], [31] are proposed, also known as the detector-free methods. These methods [12], [21], [32] perform dense feature matching over the entire image and then select confident matches, which achieve impressive matching precision. Dense matching methods [13], [33], [34] output a dense warp with confidence map for the image pair. Recent DKM [13] reformulates this framework as a Gaussian Process and achieves *state-of-the-art* performance. Our methods, *MESA* and *DMESA*, focus on reducing matching redundancy through area matching. However, they can be seamlessly combined with all three kinds of point matching methods described above to increase matching precision through the A2PM framework.

2.2 Matching Redundancy Reduction.

Matching redundancy is evident in non-overlapping areas between images, motivating several works [16], [30], [35] to focus on covisible areas extraction. They predict overlaps between images by iterative matching [30] or overlap segmentation [16], [35], [36]. Nevertheless, matching redundancy also exists inside the overlapping area, when it comes to detailed local point matching. TopicFM [17] proposes to divide image contents into topics

and then restrict matching to the same topic to avoid redundant computation. The learning-based topic inference, however, is implicit, suffering from lack of versatility and generalization issues. On the other hand, SGAM [18] explicitly finds semantic area matches between images and the matching redundancy is reduced inside the areas by semantics. Then, point matching is performed between the matched areas. This A2PM framework is simple yet effective. Our methods further build on its advantages, but leverage the advancing image segmentation method, *i.e.* SAM, to overcome the ambiguity issue from explicit semantics.

2.3 Area to Point Matching.

Establishing area matches with prominent semantics is an effective way to reduce the matching redundancy. To this end, SGAM [18] proposes the semantic area matches as an efficient intermediate search space for feature matching, along with the corresponding A2PM framework. This framework obtains informative area matches as the input of point matchers, providing greater detail within the same resolution and reducing matching noise compared to original images, contributing to accurate point matching. However, SGAM heavily relies on explicit semantic prior, leading to performance sensitivity to semantic labeling precision and scene semantic granularity. In contrast, *MESA/DMESA* utilize pure image segmentation, *i.e.* SAM results, for area matching, which is more practical and remedies drawbacks associated with explicit semantics. Meanwhile, based on the impressive image understanding capability of SAM, the area matches established by *MESA/DMESA* possess implicit semantics, facilitating matching redundancy reduction, similar to areas with explicit semantics.

3 PRELIMINARIES: A2PM

MESA and *DMESA* both adhere to the Area to Point Matching (A2PM) framework [18], which is a foundation of our work. To begin with, we revisit the A2PM framework briefly in Sec. 3.1. Then, due to the pivotal role of image resolution in A2PM, we analyse its effect in feature matching (Sec. 3.2). Based on this, we carefully offer a detailed resolution configuration of A2PM and discuss its motivation (Sec. 3.3), which is vague in [18].

3.1 Overview of A2PM

The initial motivation behind the A2PM framework is to refine the search space for feature matching using semantics [18]. To this end, a semantic-friendly search space was proposed, known as the semantic area match. By matching these areas, redundancy in feature matching between images could be effectively eliminated by semantic, and these area pairs could also provide more local details to the point matcher. Then, the A2PM framework was introduced, which focuses on the coupling of area matching (AM) and point matching (PM). In this framework, the semantic area matches $\{(a_0^i, a_1^i)\}_i$ are first established by AM between image pairs (I_0, I_1) , followed by PM within these area pairs cropped from original images. Finally, fusing the inside-area point matches yields the ultimate results \mathcal{P} (the correspondences).

$$\mathcal{P} \stackrel{fuse}{\leftarrow} \{PM(a_0^i, a_1^i)\}_i \stackrel{crop}{\leftarrow} AM(I_0, I_1). \quad (1)$$

This flexible combination enables independent development of AM techniques to improve the matching precision of various PM methods. Evidently, accurate AM is the basis of A2PM. Our *MESA* and *DMESA* thus focus on the precise AM, and showcase consistent improvement for sparse, semi-dense and dense point matchers in extensive experiments.

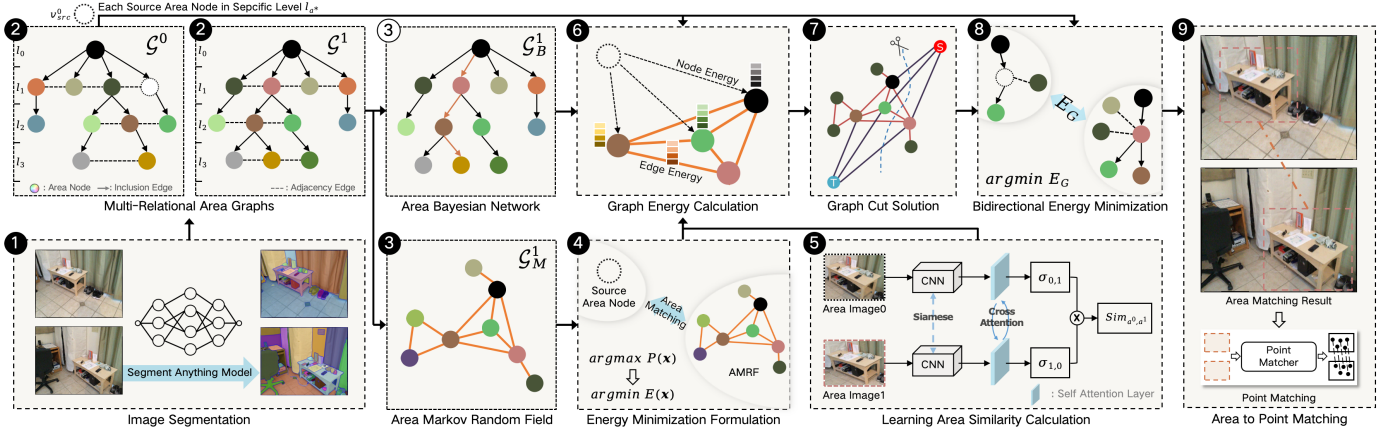


Fig. 3. **Overview of MESA.** Based on ① *SAM segmentation*, we first construct ② *Area Graphs*. Then the graph is turned to two graphical models based on its two different edges. Through ④ *Area Markov Random Field*, area matching is formulated as an ④ *Energy Minimization*. Meanwhile, leveraging ③ *Area Bayesian Network* and our ⑤ *Learning Area Similarity Calculation*, ⑥ *Graph Energy* can be efficiently calculated. Therefore, ⑦ *Graph Cut* is utilized to obtain putative area matches. Finally, ⑧ *Bidirectional Energy Minimization* determines the best area match, which serves as the input of subsequent point matcher for precise feature matching, following the ⑨ *Area to Point Matching* framework [18].

3.2 Image Resolution Impact in Feature Matching

In A2PM, three resolutions are involved, including the *original image resolution*, *area image resolution*, and *input PM resolution*. Determining these resolutions is non-trivial in this framework. While image resolution significantly impacts feature matching, discussions on this subject are limited. This motivates us to discuss the influence of image resolution on matching performance here and experimentally investigate the impact in Sec. 6.

Resolution variation impacts feature matching in three primary ways. 1) Resolution essentially reflects the level of *detail* preserved in images and higher resolution enhances matching accuracy. However, increasing resolution also raises computational demands, making resolution selection a balance between accuracy and efficiency in practice. 2) Changes in image resolution can lead to changes in *aspect ratio*, causing *distortion* in image content that can reduce matching accuracy. 3) Learning-based methods frequently demonstrate *overfitting to the training resolution*. Especially for semi-dense matchers, resolution variation can lead to significant performance declines (cf. Sec. A of the appendix), due to their Transformer-based structure [37].

3.3 Image Resolution Configuration in A2PM

Based on the above findings, we offer detailed resolution settings for A2PM. Specifically, the original image resolution is set to the resolution of the raw images in the dataset. The resolution of area images and PM input share the same aspect ratio, which is set as 1. Therefore, in A2PM, the specific cropping operation *first expands* the shorter side of areas to form squares, *then crops* them from the high-resolution original image, and finally scale them to the required and square input resolution.

The reasons for the settings are as follows. 1) Due to the accurate AM of our methods, matching redundancy is sufficiently reduced in area images. Thus, most of the inside-area pixels containing useful details for PM. Cropping areas from the high-resolution original image preserves these details as much as possible, thereby benefiting the point matching. 2) The same aspect ratio between area images and PM input avoid distortion during re-size. 3) The aspect ratio constraint of 1 arises from the uncertainty in semantic area sizes. In other words, the sizes of the semantic areas are determined by specific semantics, whose aspect ratios

vary across different images. However, point matchers require input image pairs to have the same dimensions. Therefore, we set a uniform input resolution with aspect ratio of 1, which leads to minimizes changes in area size in a statistical sense, reducing the disruption to matching redundancy reduction achieved by AM.

Next, we discuss the impact of learning resolution overfitting on A2PM. When the training resolution has an aspect ratio of 1, this overfitting is harmless. Based on accurate AM, A2PM framework can provide superior inputs for point matchers, thus improving matching accuracy. Conversely, when the training aspect ratio deviates from 1, the performance of A2PM method using square inputs is inferior to original PM with training size, due to the overfitting issue. Meanwhile, using the training resolution as the input PM size in A2PM still leads to a decrease in matching performance due to excessive area size adjustments. However, in experiments (cf. Tab. 3), we **only** observe the drop in performance specifically with *Transformer-based methods* on the *in-domain dataset*, corresponding to the severe overfitting issues of these methods. To alleviate this issue, we can fine-tune the models on square resolution (cf. Sec. 6.6). However, this technique, while effective, entails additional training expenses. The optimal approach should focus on addressing the overfitting issue in Transformer. We hope that this will inspire additional progress in PM within the community.

4 SPARSE AREA MATCHING

In this section, we introduce the sparse AM approach, called *MESA*, which leverages SAM to effectively establish area matches between images. MESA employs a sparse pipeline for AM: it initially identifies candidate areas in images and subsequently matches these candidates, akin to sparse PM. There are two main components in MESA: the *Area Graph* (AG)(Sec. 4.1) and the *Graphical Area Matching* (Sec. 4.2). The former is a graph structure that describes global area relations to extract areas and serves as a basis for AM. The later is responsible for finding area matches utilizing both the constructed spatial relations and local features of these areas.

4.1 Area Graph

The main motivation to propose the AG is that direct AM on SAM results is inaccurate, as global information is ignored in

independent areas. Meanwhile, fixed area sizes hinder robust PM under scale changes. Hence, AG is designed to capture the global structure of these areas and construct scale hierarchy for them, contributing to accurate and robust AM. Next, we first introduce the concept of AG in Sec. 4.1.1 and then explain how to construct the AG from the SAM [14] results of an image in Sec. 4.1.2.

4.1.1 Area Graph Definition

The AG ($\mathcal{G} = \langle \mathcal{V}, \mathcal{E} \rangle$) takes image areas as nodes and contains two edges to model inter-area relations (Fig. 4), thus making it a *multi-relational graph* [38]. The graph nodes include both areas provided by SAM and areas generated by graph completion (cf. Sec. 4.1.2). We divide these areas into L levels according to their sizes, corresponding to different image scales, to serve as the foundation of area scale hierarchy. On the other hand, the graph edges ($\mathcal{E} = \mathcal{E}_{in} \cup \mathcal{E}_{adj}$) represent two relations between areas, *i.e.* inclusion (\mathcal{E}_{in}) and adjacency (\mathcal{E}_{adj}). The inclusion edge $e_{in} \in \mathcal{E}_{in}$ is directed, pointing from an area to one of its containing areas. It forms a hierarchical connection between graph nodes, enabling robust and efficient AM especially under scale changes. The adjacency edge $e_{adj} \in \mathcal{E}_{adj}$ is undirected, indicating the areas it connects share common parts but without the larger one including the smaller one. This edge captures the spatial relations between areas, beneficial to accurate AM. By the above two edges, AG models both the spatial and scale structure of image areas, playing an fundamental role in MESA.

4.1.2 Area Graph Construction

The construction of AG includes collecting areas as nodes and connecting them by proper edges. Not all SAM areas can function as nodes, since some are too small or have extreme aspect ratios, rendering them unsuitable for PM. Thus, **Area Pre-processing** is performed first to obtain initial graph nodes. We then approach the edge construction as a **Graph Link Prediction** problem [39]. Afterwards, the preliminary AG is formed, but it still lacks matching efficiency and scale robustness. Thus, we propose the **Graph Completion** algorithm, which generates additional nodes and edges to construct the scale hierarchy.

Area Pre-processing: To filter unsuitable areas, we set two criteria: the acceptable minimal area size (T_s) and maximum area aspect ratio (T_r). Any area that has smaller size than T_s or larger aspect ratio than T_r , gets screened out. The remaining areas are added into the candidate areas set. For each filtered area, we fuse it with its nearest neighbor area in the candidate set. We repeat the filtering and fusion on the candidate set until no areas get screened out. Then, we assign a level l_a to each candidate area a based on its size, by setting L size thresholds ($\{TL_i \mid i \in [0, L - 1]\}$):

$$l_a = i \mid TL_i \leq W_a \times H_a < TL_{i+1}. \quad (2)$$

The size level is the basis of scale hierarchy in AG.

Graph Link Prediction: The edge construction is treated as a link prediction problem [39]. Given two area nodes (v_i, v_j), the edge between them (e_{ij}) can be predicted according to the spatial relation of their corresponding areas (a_i, a_j). This approach adopts the ratio of *the overlap size* (O_{ij}) to *the minimum area size* between two areas ($\delta = O_{ij} / \min(W_i \times H_i, W_j \times H_j)$) as the score function:

$$e_{ij} \in \begin{cases} \mathcal{E}_{in} & , \delta \geq \delta_h \\ \mathcal{E}_{adj} & , \delta_l < \delta < \delta_h \\ \emptyset & , \delta \leq \delta_l \end{cases}, \quad (3)$$

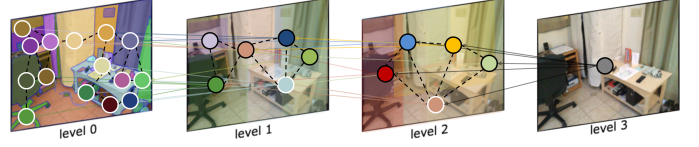


Fig. 4. **The proposed Area Graph.** The graph nodes (circles with masks representing rectangle areas) includes both areas from SAM results (white boundaries) and our graph completion algorithm (black boundaries). They are divided into four levels according to their sizes. The adjacency edges (dashed lines) and inclusion edges (arrows) connect all nodes. Only adjacency edges within the same level are shown for better view.

where δ_l, δ_h are predefined thresholds.

Graph Completion: Initial AG is achieved by connecting all processed nodes with different edges. However, since SAM inherently produces areas containing complete entity, there are few inclusion relations among areas. Consequently, initial AG lacks the scale hierarchy, which reduces its robustness at scale variations and makes accessing nodes inefficient. To address the issue, we propose the *Graph Completion* algorithm, which generates additional nodes and edges to ultimately construct a tree structure in the original graph. The core of this algorithm is to generate parent nodes for each orphan node, *i.e.* the node has no parent node in the next higher level, from small to large size levels. The algorithm begins at the smallest level, collects all orphan nodes, and clusters them based on their center coordinates. Nodes in the same cluster have their corresponding areas fused with their nearest neighbors. It is noteworthy that these generated areas containing multiple objects preserve the internal implicit semantic. Based on our level thresholds, the resulting areas correspond to new higher level nodes. If a node remains single after clustering, we increase its area size to the next level to allow for potential parent nodes. We repeat the above operations on each level and connect generated nodes to others by suitable edges. More details can be found in the Sec. C of the appendix.

4.2 Graphical Area Matching

In this part, we describe our AM method, which formulates AM on the graph, based on two graphical models derived from the AG. Given two AGs ($\mathcal{G}^0, \mathcal{G}^1$) of the input image pair (I_0, I_1) and one area ($a_{src}^0 \in I_0$) corresponding to node $v_{src}^0 \in \mathcal{G}^0$ (termed as the *source node*), AM involves finding the node $v_j^1 \in \mathcal{G}^1$ with the highest probability of matching its corresponding area a_j^1 to the source node area a_{src}^0 . However, treating this problem as independent node matching is inadequate, as which disregards global information between areas modeled in AG by its two edges. Meanwhile, the two edges respectively convert AG into two graphical models, *i.e.* Markov Random Fields (undirected edges) and Bayesian Network (directed edges). These observations naturally motivate us to formulate the AM task inside a framework of graphical model.

In the following, we first introduce the undirected graph from AG, named Area Markov Random Field (AMRF, Sec. 4.2.1), which converts the AM task into an energy minimization task. To calculate the local matching energy between areas, we propose a learning model in Sec. 4.2.2 to achieve area similarities based on inside-area features. Then, the directed graph from AG, termed as Area Bayesian Network (ABN, Sec. 4.2.3) is presented to avoid redundant energy calculation. Finally, to achieve the best area match, an energy-based refinement is proposed (Sec. 4.2.4), by considering graph structures of both input images.

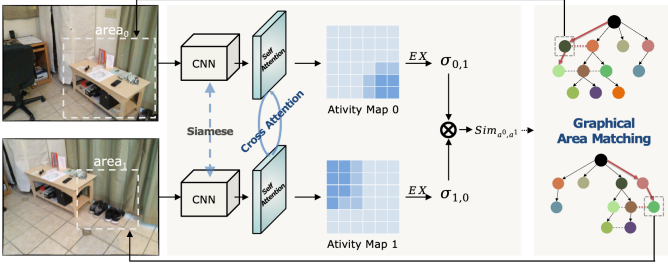


Fig. 5. **Learning area similarity.** The area similarity calculation is formed as the patch-level classification. We predict the probability of each patch in one area appearing on the other to construct activity maps. The similarity is obtained by the product of activity expectations, contributing to our exact AM.

4.2.1 Area Markov Random Field

The adjacency edge in AG implies the correlation between probabilities of two nodes matching the source node. By considering the general adjacency relation, which includes the inclusion relations as adjacency too, the \mathcal{G}^1 is transformed into an undirected graph. Next, random variables (\mathbf{x}) are introduced for all nodes to indicate their matching status with the source node. The binary variable $x_i \in \mathbf{x}$ is equal to 1 when v_i^1 matches v_{src}^0 and 0 otherwise. Therefore, the AMRF ($\mathcal{G}_M^1 = \langle \mathcal{V}, \mathcal{E}_{adj} \rangle$) is obtained and AM can be performed by maximizing the joint probability distribution over the AMRF:

$$\arg \max_{\mathbf{x}} P(\mathbf{x}). \quad (4)$$

Based on the *Hammersley-Clifford* theorem [40], the probability distribution defined by AMRF belongs to the *Boltzmann distribution*, which is an exponential of negative energy function ($P(\mathbf{x}) = \exp(-E(\mathbf{x}))$). Therefore, the AM can be formulated as an energy minimization.

$$\arg \min_{\mathbf{x}} E(\mathbf{x}). \quad (5)$$

The energy can be divided into two parts, *i.e.* the energy of nodes ($E_{\mathcal{V}}$) and edges ($E_{\mathcal{E}}$), based on the graph structure.

$$E(\mathbf{x}) = \sum_i E_{\mathcal{V}}(x_i) + \lambda \sum_{(i,j) \in \mathcal{N}} E_{\mathcal{E}}(x_i, x_j), \quad (6)$$

where λ is a parameter balancing the terms and \mathcal{N} is the set of all pairs of neighboring nodes. For each graph node v_i^1 , its energy is expected to be low when its matching probability is high, which can be reflected by the apparent similarity ($S_{a_{src}^0 a_i^1}$) between a_{src}^0 and a_i^1 .

$$E_{\mathcal{V}}(x_i) = |x_i - S_{a_{src}^0 a_i^1}|. \quad (7)$$

The edge energy aims to penalize all neighbors with different labels, and the Potts model [41] (T) would be a justifiable choice. To better reflect the spatial relation, the Potts interactions are specified by *IoU* [42] of neighboring areas.

$$E_{\mathcal{E}}(x_i, x_j) = IoU(a_i^1, a_j^1) \cdot T(x_i \neq x_j). \quad (8)$$

Function $T(\cdot)$ is 1 if the argument is true and 0 otherwise. Finally, the AM is formulated as an binary labeling energy minimization. By carefully defining the energy function, the energy minimization problem in Eq. (5) is efficiently solvable via the *Graph Cut* algorithm [22], [43]. The obtained minimum cut of the graph \mathcal{G}_M^1 is the matched node set ($\{v_h^1 | h \in \mathcal{H}\}$). Although the set may contain more than one area node, the best matching result can be achieved from this set by our refinement algorithm (cf. Sec. 4.2.4).

4.2.2 Learning Area Similarity

The proposed *Graph Cut* solution relies on graph energy calculations for both nodes and edges. Unlike easily available area pair *IoUs* for $E_{\mathcal{E}}$, determining the area apparent similarity for $E_{\mathcal{V}}$ is not straightforward. Thus, we turn to the learning-based framework, inspired by recent successes of learning models in PM [11], [12], [44]. One simple idea is to calculate the correlation of learning descriptors of two areas [44] as the area similarity. However, the descriptor correlation is too rough for accurate AM and lacks fine-grained interpretability. To overcome these issues, we decompose the area similarity calculation into two patch-level classification problems as shown in Fig. 5.

Specifically, for each image in the area image pair $\{a_j | j \in \{0, 1\}\}$ reshaped to the same size, we perform binary classification for each $1/8 \cdot W_{a_j} \times 1/8 \cdot H_{a_j}$ image patch p_i^j (where i is the index of patch and j is the index of area image) in it, computing the probability of p_i^j appearing on the other area image, termed as the patch activity σ_i^j . To accomplish the classification, we first extract patch-wise features from each area image using a Siamese CNN [45]. Then we update these patch features via self and cross-attention with normalization [46], resulting in patch activities. Utilizing these patch activities, we construct an activity map ($\sigma_m^j = \{\sigma_i^j | j \in \{0, 1\}\}_i$, where i is the index of element in this set) for each area image. When two areas are ideally matched, the corresponding 3D point of every pixel in one area is projected onto the other area. Hence, all the patch activities of both areas should be closed to 1, revealing the area similarity can be represented by the product of expectations of two activity maps, $EX(\sigma_m^i) = \sigma_{i,j}$, where $i \neq j$, $i, j \in \{0, 1\}$.

$$Sim_{a^0, a^1} = EX(\sigma_m^0) \times EX(\sigma_m^1) = \sigma_{0,1} \times \sigma_{1,0}. \quad (9)$$

Through this approach, the calculation of area similarity is transformed into the patch-level classification, which enhances the interpretability and accuracy of AM.

4.2.3 Area Bayesian Network

Although the *Graph Cut* can be performed in polynomial time [43], the dense energy calculation over \mathcal{G}_M^1 is time consuming. Furthermore, due to the scale hierarchy in AG, this dense calculation is highly redundant. In particular, if the area a_{src}^0 is not matched to a_j^1 , it won't be matched to any children area of a_j^1 . This observation reveals the conditional independence in the similarity calculation, which involves inclusion edges in \mathcal{G}^1 , thus turning \mathcal{G}^1 to a Bayesian Network (\mathcal{G}_B^1) [47]. Therefore, the redundancy in the similarity calculation can be reduced. In practice, we calculate the dense similarities by constructing a similarity matrix $M_S \in \mathbb{R}^{|\mathcal{V}^0| \times |\mathcal{V}^1|}$. Note *not* all similarities in M_S need calculation, but any similarity can be accessed in M_S . We first calculate similarities related to all source nodes. Subsequent calculations are saved in M_S as well. For $M_S[i, j]$ that has not been calculated, we achieve it by our learning model (cf. Sec. 4.2.2):

$$M_S[i, j] = Sim_{a_i^0, a_j^1}. \quad (10)$$

If $M_S[i, j] < T_{as}$, all children nodes $\{v_h^0 | h \in ch^0(i)\}$ and $\{v_c^1 | c \in ch^1(j)\}$ of v_i^0 and v_j^1 are found from \mathcal{G}_B^0 and \mathcal{G}_B^1 , where $ch^j(i)$ is the index set of children indices of node v_i^j from \mathcal{G}_B^j . Based on the conditional independence, we have:

$$M_S[h, k] = 0, \quad \forall (h, k) \in ch^0(i) \times ch^1(j). \quad (11)$$

This operation effectively reduce the times of similarity calculation, leading to more efficient AM.

4.2.4 Bidirectional Matching Energy Minimization

The minimum cut $\{v_h^1 | h \in \mathcal{H}\}$ achieved through the *Graph Cut* may contain more than one area node, indicating further refinement is necessary to obtain the best area match. Moreover, the aforementioned *graphical area matching*, i.e. finding the corresponding area node in \mathcal{G}^1 for $v_{src}^0 \in \mathcal{G}^0$, only considers the structure information in \mathcal{G}^1 and ignores the structure of \mathcal{G}^0 . To overcome this limitation, we propose a bidirectional matching energy E_G for each candidate node v_h^1 , consisting of four parts:

$$E_G(v_h^1) = \frac{1}{Z} (\mu \cdot E_{self}(v_h^1) + \alpha \cdot E_{parent}(v_h^1) + \beta \cdot E_{children}(v_h^1) + \gamma \cdot E_{neighbour}(v_h^1)), \quad (12)$$

where μ, α, β and γ are weights to balance the terms; Z is the partition function. The $E_{self}(v_h^1)$ is the energy related to matching probability between v_{src}^0 and v_h^1 :

$$E_{self}(v_h^1) = |1 - Sim_{a_{src}^0, a_h^1}|. \quad (13)$$

The $E_{parent}(v_h^1)$ is the energy related to matching probability between the parent node pairs of v_{src}^0 and v_h^1 :

$$E_{parent}(v_h^1) = \min\{|1 - Sim_{a_u^0, a_r^1}| | u \in p^0(src), r \in p^1(h)\}, \quad (14)$$

where $p^i(j)$ is the index set of parent nodes of v_j^i in \mathcal{G}_i . This energy is the minimum matching energy among all parent node pairs of v_h^1 and v_{src}^0 . Same as the E_{parent} , the $E_{children}$ and $E_{neighbour}$ are the energy parts of children and neighbour node matching pairs. Afterwards, the best area match $v_{h^*}^1$ in the set can be found by minimize E_G :

$$h^* = \arg \min_{h \in \mathcal{H}} E_G(v_h^1). \quad (15)$$

If the $E_G(v_{h^*}^1) > T_{E_{max}}$ (a threshold parameter), the source area node v_{src}^0 is considered to have no matches. To further improve the accuracy of final match, we set an energy range threshold T_{Er} to collect all the candidates within a certain energy range.

$$\{v_h^1 | |E_G(v_h^1) - E_G(v_{h^*}^1)| \leq T_{Er}, \bar{h} \in \mathcal{H}\}. \quad (16)$$

Then the final area match is achieved by fusing $v_{h^*}^1$ and all candidates $\{v_h^1\}_{\bar{h}}$ with E_G as weights, similar to [44]. This refinement completely considers the structure information of both \mathcal{G}^0 and \mathcal{G}^1 and achieves exact area matches.

5 DENSE AREA MATCHING

Sparse area matching, i.e. MESA, is robust and precise. Nonetheless, its primary drawbacks are efficiency-related, mainly stemming from the numerous repetitive similarity calculations. To address the limitation, we propose a more flexible and faster AM method, named *DMESA*, which matches semantic areas from SAM in a dense manner and requires no training. The core of DMESA involves deriving area matches from patch correspondences, which can be established through the coarse-level matching of an off-the-shelf point matcher [12]. Particularly, after source area image is obtained from the AG, DMESA first establishes patch matches between the area and the target image. Then a matching distribution is generated on the target image (Sec. 5.1) to guide AM, by formulating the patch matches as a Gaussian

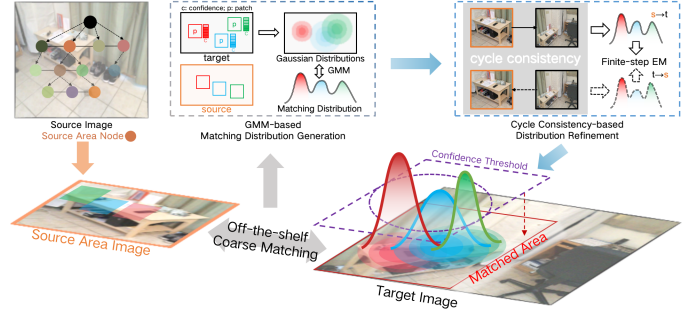


Fig. 6. **Overview of DMESA.** DMESA derives area matches from dense patch matches between the source area image and the target image, obtained through an off-the-shelf coarse matching. We model the patch matches utilizing GMM to render a confidence map in the target image, where the cycle-consistency can be introduced by a finite-step EM algorithm for refinement. Then, the area matches can be efficiently attained by applying a confidence threshold.

Mixture Model (GMM). To further migrate the coarse accuracy issue, the cycle-consistency refinement is proposed (Sec. 5.2). Based on the matching consistency prior [23], this refinement employs Expectation Maximization (EM) algorithm with finite steps to ultimately enhance the AM precision.

5.1 Matching Distribution Generation

The basis of DMESA is to generate a dense matching distribution to guide AM leveraging patch matches. To this end, we first establish patch matches ($\{p_k\}_k^K$) between the source area and the target image, along with their *confidences*. This can be easily achieved by utilizing the coarse matching stage of an off-the-shelf point matcher [12]. Then, the patch matches can be treated as Gaussian distributions in the target image; the patch centers ($\{u_k, v_k\}_k^K$) are the means ($\{\mu_k\}_k^K$) and the match confidence ($\{c_k\}_k^K$) can be used to generate variance ($\{\Sigma_k\}_k^K$):

$$\mu_k = (u_k, v_k), \quad \Sigma_k = \begin{bmatrix} \frac{w_{p_k}}{c_k} & 0 \\ 0 & \frac{h_{p_k}}{c_k} \end{bmatrix}, \quad (17)$$

where $w_{p_k} \times h_{p_k} = 8 \times 8$ is the size of the patch p_k . Afterwards, we can get multiple Gaussian distributions in the target image, representing the matching probabilities of 2D locations ($\{x_k \in p_k\}_k$) inside the patches.

$$p(x_k) = \frac{1}{2\pi |\Sigma_k|^{\frac{1}{2}}} \exp -\frac{1}{2} (x_k - \mu_k)^T \Sigma_k^{-1} (x_k - \mu_k) = \mathcal{N}_k(x_k | \mu_k, \Sigma_k). \quad (18)$$

Therefore, we can model the joint matching distribution in the target image as a GMM, by introducing an one-hot K -dimensional latent variable z and $p(z) = \prod_k^K \pi_k z_k^k$, where z_k represents the k -th entry of the vector z and π_k is the mixing coefficients [47].

$$p(x) = \sum_k^K \pi_k \mathcal{N}(x_k | \mu_k, \Sigma_k). \quad (19)$$

This matching distribution can guide the AM. By setting a specific confidence threshold T_c , the potential boundary points of the area ($p(x) = T_c$) can be obtained from the distribution. The matched area in the target image, thus, can be achieved as the bounding box of these boundary points.

5.2 Cycle-consistency Refinement

Utilizing patch matching is an economical way to obtain area matches, but the inherently coarse nature of patches limits their accuracy, subsequently restricting the precision of the resulting area matches. This motivates us to further refine the AM distribution. In particular, we improve the precision of AM distribution by introducing the cycle-consistency prior. Cycle-consistency is a common constraint in matching [23], [48], stating that correct matches should not be influenced by the matching direction, which refers to the selection of source and target images. The coarse matching method [12] employed in DMESA operates asymmetrically on input image pairs. It only searches for correspondences in the target image for patches in the source image. Thus, the cycle-consistency prior can be introduced by exchanging the source and target images in this coarse matching. Specially, following the probability form in Sec. 5.1, coarse matching achieves the joint distribution $p(\mathbf{x}^{s \rightarrow t}; \{\boldsymbol{\mu}_k^{s \rightarrow t}\}_k^K, \{\boldsymbol{\Sigma}_k^{s \rightarrow t}\}_k^K)$ (Eq. 19) for AM. After modifying the matching direction, another distribution can be obtained: $p(\mathbf{x}^{t \rightarrow s}; \{\boldsymbol{\mu}_k^{t \rightarrow s}\}_k^K, \{\boldsymbol{\Sigma}_k^{t \rightarrow s}\}_k^K)$. Since the key insight is the consistency between two matching directions, we can enforce the fusion of above two distributions to achieve the consistent matching results. Therefore, we propose a finite-step EM algorithm to fuse the two distributions.

There are two important elements in the EM algorithm applied to GMM: the observed data and the initial parameters to be updated. In this case, we can sample data from the distribution $p(\mathbf{x}^{s \rightarrow t})$ as the observation $\mathbf{x}^{s \rightarrow t}$ and set $\{\boldsymbol{\mu}_k^{t \rightarrow s}\}_k^K, \{\boldsymbol{\Sigma}_k^{t \rightarrow s}\}_k^K$ as initial parameters $\theta_0^{t \rightarrow s}$. Then, we can use the EM equation [47] to update the parameters:

$$\theta_{t+1}^{t \rightarrow s} = \arg \max_{\theta} \int \log p(\mathbf{x}^{s \rightarrow t}, \mathbf{z} | \theta^{t \rightarrow s}) p(\mathbf{z} | \mathbf{x}^{s \rightarrow t}, \theta^{t \rightarrow s}) dx, \quad (20)$$

where $p(\mathbf{z}) = \prod_k^K \pi_k^{z_k}$ and $\{\pi_k\}_k^K$ are initialized as $\pi_k = \frac{1}{K}$. After a finite number of update steps ($t = S_{EM}$), we use the updated parameters $\theta_{S_{EM}}^{t \rightarrow s}$ including means and variances to generate the refined patch matches. Thus, more accurate matching distribution, admitted by both matching directions, can be achieved, ultimately increase the AM precision. Note the matched patches are established in the source area as well. Thus, we can refine the source area by above techniques at the same time.

6 EXPERIMENTS

In this section, we comprehensively evaluate our methods on feature matching and its downstream tasks. Firstly, the implementation details of our methods are presented in Sec. 6.1. Then, experiment results on the area and point matching task are reported in Sec. 6.2 and Sec. 6.3. Next, extensive pose estimation experiments (Sec. 6.4) are conducted on various datasets. Additionally, we perform visual odometry (Sec. 6.5) to showcase the performance of our methods in driving scenes. The impact of input resolution variation, PM model fine-tuning and data domain shift are experimentally investigated in Sec. 6.6 and Sec. 6.7. Further ablation studies of MESA and DMESA are provided in Sec. 6.8.

6.1 Implementation Details

This section describes the implementation details of our method in three aspects, corresponding to three core elements of the A2PM framework: AM, PM, and the integration of these two parts.

TABLE 1

Area matching results. We compare the area matching performance between SGAM, MESA and DMESA, combined with GAM [18] under various ϕ settings. Results of each series are highlighted as **best**, **second** and **third** respectively.

Method	AOR \uparrow	AMP@0.6 \uparrow	ACR \uparrow	Pose AUC@5 \uparrow
SGAM [†] [18]+SP+SG [9]	50.37	46.76	80.45	19.15
w/ GAM ($\phi = 0.5$)	54.87	50.22	67.54	19.32
w/ GAM ($\phi = 1.0$)	60.36	53.47	71.31	20.54
w/ GAM ($\phi = 3.5$)	59.74	52.31	73.42	20.27
MESA+SP+SG	65.12	77.89	94.93	20.33
w/ GAM ($\phi = 0.5$)	62.34	75.56	71.65	19.97
w/ GAM ($\phi = 1.0$)	67.45	80.24	85.22	21.22
w/ GAM ($\phi = 3.5$)	68.44	83.25	94.57	22.72
DMESA+SP+SG	71.36	82.56	85.52	19.97
w/ GAM ($\phi = 0.5$)	72.46	84.33	64.50	20.14
w/ GAM ($\phi = 1.0$)	75.33	85.46	69.08	21.23
w/ GAM ($\phi = 3.5$)	78.13	86.45	79.44	22.19

[†] SGAM with only semantic area matching activated.

6.1.1 Details of AM

The AM phase contains the proposed MESA and DMESA. We offer the **parameter settings** of both methods here, along with the **training details** of the learning area similarity model in MESA.

Parameter settings: For MESA, the common parameters for different scenes are set as follows. In AG construction, the input image are resized to 640×480 . The aspect ratio threshold $T_r = 4$ and minimal size threshold is $T_s = 80^2$. The number of area size threshold is 4 and specific T_{Lis} are $80^2, 130^2, 256^2, 390^2, 560^2$. The δ_l is 0.1 and δ_h is 0.8. In graphical area matching, the λ in Eq. (6) is 0.1. The area similarity threshold $T_{as} = 0.05$. The energy balance weights ($\mu, \alpha, \beta, \gamma$) in Eq. (12) are 4, 2, 2, 2. The specific area level l_{a^*} for point matching is 1. The T_{Er} in Eq. (16) is 0.1. Other parameters specified for different scenes are described in experiment sections. Ablation study about the parameter settings of MESA can be found in Sec. E.2 of the appendix. **For DMESA,** the confidence threshold is empirically $T_c = e^{-1}/2\pi$ and the step number of EM is set as $S_{EM} = 1$.

Training details: We propose the learning model for area similarity calculation in MESA, whose training protocol is described as follows. Due to the classification formulation, we use the binary cross entropy [49] of each patch classification to form the loss function of area similarity calculation. Regular area images are generated using AG from both indoor and outdoor datasets [50], [51] as the training data. We train the indoor and outdoor models respectively on 2 NVIDIA RTX 4090 GPUs using AdamW [52].

6.1.2 Details of PM

As described in Sec. 3.3, model fine-tuning is able to increase matching accuracy in specific input sizes. However, this process incurs additional training costs. Therefore, to demonstrate the efficacy of our methods in a practical manner, we utilize the **original models** of point matchers provided by their authors in the following experiments, unless explicitly stated otherwise.

6.1.3 Details of A2PM

The A2PM framework is responsible for the integration between AM and PM, including the **area image cropping** (from AM results to PM input) and **match fusion** (from inside-area PM results to final matches).

Area image cropping: As described in Sec. 3.3, we crop area images with a specified aspect ratio ($r_a := W/H$, usually set as

TABLE 2

Point Matching on ScanNet1500. Relative gains are highlighted as subscripts. The **best**, **second** and **third** results are highlighted.

Image Matching	640 × 640			640 × 480 [†]			480 × 480			
	MMA@5 [†]	MMA@10 [†]	MMA@20 [†]	MMA@5 [†]	MMA@10 [†]	MMA@20 [†]	MMA@5 [†]	MMA@10 [†]	MMA@20 [†]	
Sparse	SP [5]+SG [9]	20.50	38.22	51.84	20.61	38.46	51.82	20.53	38.25	51.56
	SGAM [18]+SP+SG	21.37 _{+4.24%}	40.85 _{+6.88%}	53.61 _{+3.41%}	21.75 _{+5.53%}	40.23 _{+4.60%}	52.81 _{+1.91%}	22.71 _{+10.62%}	40.45 _{+5.75%}	52.21 _{+1.26%}
	MESA+SP+SG	24.62 _{+20.10%}	43.18 _{+12.98%}	56.29 _{+8.58%}	25.79 _{+25.13%}	44.86 _{+16.64%}	57.81 _{+11.56%}	25.34 _{+23.43%}	44.02 _{+15.08%}	56.87 _{+10.30%}
	DMESA+SP+SG	22.89 _{+11.66%}	41.12 _{+7.59%}	54.29 _{+4.73%}	22.89 _{+11.06%}	41.13 _{+6.94%}	54.17 _{+4.53%}	23.46 _{+14.27%}	41.96 _{+9.70%}	55.03 _{+6.73%}
Semi-Dense	ASpan [12]	25.13	47.02	62.34	27.50	49.13	63.65	18.97	37.80	52.94
	SGAM+ASpan	25.59 _{+1.83%}	47.64 _{+1.32%}	62.75 _{+0.66%}	24.51 _{-10.87%}	45.95 _{-6.47%}	62.27 _{-2.17%}	20.97 _{+10.54%}	38.18 _{+1.01%}	53.19 _{+0.47%}
	MESA+ASpan	26.20 _{+4.26%}	48.94 _{+4.08%}	63.88 _{+2.47%}	25.60 _{-6.91%}	46.82 _{-4.70%}	61.63 _{-3.17%}	22.19 _{+16.97%}	42.17 _{+11.56%}	57.14 _{+7.93%}
	DMESA+ASpan	28.78 _{+14.52%}	51.06 _{+8.59%}	65.45 _{+4.99%}	26.65 _{-3.09%}	48.47 _{-1.34%}	62.99 _{-1.04%}	25.76 _{+35.79%}	46.71 _{+23.57%}	60.97 _{+15.17%}
Semi-Dense	QT [21]	22.85	41.78	53.43	29.87	52.78	67.64	24.56	45.91	61.22
	SGAM+QT	23.35 _{+2.19%}	42.13 _{+0.84%}	55.32 _{+3.54%}	30.14 _{+0.90%}	52.41 _{-0.70%}	66.38 _{-1.86%}	25.54 _{+3.99%}	46.23 _{+0.70%}	62.45 _{+2.01%}
	MESA+QT	29.32 _{+28.32%}	48.41 _{+15.87%}	60.34 _{+12.93%}	31.25 _{+4.62%}	54.73 _{+3.69%}	69.15 _{+2.23%}	26.93 _{+9.65%}	48.56 _{+5.77%}	63.79 _{+4.20%}
	DMESA+QT	24.47 _{+7.09%}	43.72 _{+4.64%}	55.44 _{+3.76%}	30.39 _{+1.74%}	53.47 _{+1.31%}	67.94 _{+0.44%}	28.72 _{+16.94%}	50.70 _{+10.43%}	65.20 _{+6.50%}
Dense	LoFTR [11]	26.47	48.99	63.75	28.18	50.68	65.43	20.08	40.22	55.86
	SGAM+LoFTR	27.15 _{+2.57%}	49.53 _{+1.10%}	65.52 _{+2.78%}	26.22 _{-6.96%}	49.13 _{-3.06%}	64.73 _{-1.07%}	21.41 _{+6.62%}	42.03 _{+4.50%}	56.73 _{+1.56%}
	MESA+LoFTR	29.97 _{+13.22%}	52.13 _{+6.41%}	66.64 _{+4.53%}	27.12 _{-3.76%}	49.63 _{-2.07%}	64.99 _{-0.67%}	22.55 _{+12.30%}	43.43 _{+7.98%}	58.64 _{+4.98%}
	DMESA+LoFTR	29.86 _{+12.81%}	51.94 _{+6.02%}	65.77 _{+3.17%}	30.29 _{+7.49%}	52.75 _{+4.08%}	66.67 _{+1.90%}	27.07 _{+34.81%}	48.48 _{+20.54%}	63.04 _{+12.12%}
Dense	DKM [13]	26.15	45.92	59.12	26.70	46.82	60.16	26.28	46.31	59.61
	SGAM+DKM	27.65 _{+5.74%}	46.58 _{+1.44%}	60.88 _{+2.98%}	27.12 _{+1.57%}	47.11 _{+0.62%}	62.21 _{+3.41%}	27.25 _{+3.69%}	47.62 _{+2.83%}	60.34 _{+1.22%}
	MESA+DKM	30.15 _{+15.30%}	50.21 _{+9.34%}	64.42 _{+8.96%}	29.67 _{+11.12%}	50.69 _{+8.27%}	64.01 _{+6.40%}	27.87 _{+6.05%}	47.85 _{+3.33%}	60.42 _{+1.36%}
DMESA+DKM	28.30 _{+8.22%}	48.81 _{+6.29%}	62.08 _{+5.01%}	28.51 _{+6.78%}	49.26 _{+5.21%}	62.77 _{+4.34%}	28.66 _{+9.06%}	49.52 _{+6.93%}	63.04 _{+5.75%}	

[†] The training size.

1) by area expansion. Specifically, we force the cropped area to possess the required aspect ratio, while trying to keep the area center unchanged. If the original area respect ratio (W_a/H_a) is larger than r_a , we fix the width W_a of area image and expand the height H_a to W_a/r_a . Otherwise, we fix the H_a and expand the W_a to $H_a \times r_a$. If the expanded area exceeds the original image, we will move its center to keep it inside the image. This cropping operation is experimentally confirmed in Sec. E.1 of the appendix.

Match fusion: The final matches can be obtained by merging the inside-area point matches. Instead of naive fusion, we adopt *Geometric Area Matching* (GAM) [18] to enhance the matching precision utilizing geometry consistency. Additionally, we also adopt the *Global Match Collection* [18] and set the occupancy ratio as 0.6, which achieves global point matches, guided by inside-area matches, to avoid matching aggregation issue.

6.2 Area Matching

Since accurate area matching is the prerequisite for the precise point matching, we first evaluate our methods for this task on ScanNet1500 [50] benchmark, which includes 1500 image pairs of indoor scenes.

6.2.1 Experimental setup

We compare the area matching precision between our methods (*i.e.* MESA and DMESA) and semantic-based SGAM [18]. The $T_{E,max}$ in MESA is 0.35. The area size is 480×480 . The impacts of GAM to all methods are also investigated, whose parameter ϕ reflects the strictness of outlier rejection. We employ the *Area Overlap Ratio* (AOR, %) and *Area Matching Precision* (AMP@0.6, %) [18] as metrics. Moreover, we propose the *Area Cover Ratio* (ACR, %), which is the coverage of the all matched areas on the entire image, to measure the completeness of area matches. To show the effect of AM on subsequent geometry task, we combine the sparse point matcher SP+SG [9] with all the AM methods to evaluate the pose estimation accuracy, using Pose AUC@5 [11].

6.2.2 Results

The results in Tab. 1 show that our methods outperform SGAM by a large gap, *e.g.*, 60.36 AOR for SGAM compared to 68.44 for MESA and 78.33 for DMESA. DMESA achieves better area matching precision compared to MESA. However, MESA exhibits a higher ACR (94.93 vs. 85.52), possibly due to its dense area comparison, which, although resource-intensive, leads to a greater number of area matches. The improved coverage of area matches enhances the validity of point matches, crucial for subsequent geometric tasks, ultimately resulting in MESA achieving the highest pose estimation accuracy. Nevertheless, the precision of DMESA is also comparable. Considering its faster speed and flexibility, it offers a better efficiency/accuracy trade-off. Additionally, GAM settings impact the precision of both area and point matches. Notably, in both MESA and DMESA, optimal performance is attained with the relaxed geometric constraint ($\phi = 3.5$), indicating the high accuracy of most area matches obtained by our methods.

6.3 Point Matching

Point matching accuracy is a direct reflection of feature matching performance. Thus, we conduct the point matching experiments on ScanNet1500.

6.3.1 Experimental setup

To showcase the versatility and effectiveness of our methods, we incorporate five PM baselines, representing all three categories of PM, into the A2PM framework as the PM module. These include a widely-used sparse matcher: SP [5]+SG [9]; three SOTA semi-dense matchers: ASpan [12], QT [21], LoFTR [11]; and a leading dense matcher: DKM [13]. For the AM part, we compare MESA, DMESA, and SGAM [18]. The Mean Matching Accuracy (MMA@5/10/20) [8] is used to measure the matching precision.

As described in Sec. 3.3, we adopt three PM input resolutions for impact investigation, including a small size (480×480), a middle size (640×480 , also the training size for our baselines) and a large size (640×640). The smaller one leads to less computational cost, while larger one possesses more details, ideally resulting in

TABLE 3

Pose Estimation on ScanNet1500. Relative gains are represented as subscripts. The **best**, **second** and **third** results are highlighted.

Pose estimation AUC		640 × 640			640 × 480 [†]			480 × 480		
		AUC@5 [†]	AUC@10 [†]	AUC@20 [†]	AUC@5 [†]	AUC@10 [†]	AUC@20 [†]	AUC@5 [†]	AUC@10 [†]	AUC@20 [†]
Sparse	SP [5]+SG [9]	20.22	39.62	57.80	20.20	38.87	56.86	19.27	38.06	56.26
	SGAM [18]+SP+SG	21.42 _{+5.93%}	40.61 _{+2.50%}	58.34 _{+0.93%}	21.97 _{+8.76%}	39.94 _{+2.75%}	57.91 _{+1.85%}	20.54 _{+6.59%}	38.87 _{+2.13%}	57.48 _{+2.17%}
	MESA+SP+SG	23.42 _{+15.83%}	42.79 _{+8.00%}	61.49 _{+6.38%}	23.24 _{+15.05%}	42.35 _{+8.95%}	60.04 _{+5.59%}	22.72 _{+17.90%}	42.25 _{+11.01%}	59.51 _{+5.78%}
	DMESA+SP+SG	22.60 _{+11.77%}	41.31 _{+4.27%}	59.07 _{+2.20%}	21.97 _{+8.76%}	40.88 _{+5.17%}	58.71 _{+3.25%}	22.19 _{+15.15%}	41.25 _{+8.38%}	58.79 _{+4.50%}
Semi-Dense	ASpan [12]	24.48	43.64	60.38	28.37	49.24	66.44	22.43	41.67	60.26
	SGAM+ASpan	25.13 _{+2.66%}	44.27 _{+1.44%}	60.98 _{+0.99%}	26.14 _{-7.86%}	46.85 _{-4.85%}	62.72 _{-5.60%}	23.78 _{+6.02%}	42.25 _{+1.39%}	60.93 _{+1.11%}
	MESA+ASpan	25.87 _{+5.68%}	46.43 _{+6.39%}	62.47 _{+3.46%}	28.23 _{-0.49%}	49.33 _{+0.18%}	67.04 _{+0.90%}	24.56 _{+9.50%}	44.37 _{+6.48%}	61.29 _{+1.71%}
	DMESA+ASpan	25.79 _{+5.19%}	45.19 _{+3.55%}	62.18 _{+2.98%}	26.36 _{-7.08%}	46.60 _{-5.36%}	63.92 _{-3.79%}	24.25 _{+8.11%}	44.07 _{+5.76%}	62.20 _{+3.22%}
	QT [21]	22.40	40.10	56.90	28.56	49.30	65.78	21.56	40.95	57.93
	SGAM+QT	23.71 _{+5.85%}	41.55 _{+3.62%}	56.13 _{-1.35%}	26.25 _{-8.09%}	44.63 _{-9.47%}	62.73 _{-4.64%}	22.79 _{+5.71%}	42.04 _{+2.66%}	58.20 _{+0.47%}
	MESA+QT	24.12 _{+7.68%}	43.03 _{+7.31%}	60.13 _{+5.68%}	28.74 _{+0.63%}	49.12 _{-0.37%}	66.03 _{+0.38%}	24.72 _{+14.66%}	43.57 _{+6.40%}	60.41 _{+4.28%}
	DMESA+QT	23.41 _{+4.51%}	41.70 _{+3.99%}	59.14 _{+3.94%}	26.51 _{-7.18%}	46.71 _{-5.25%}	63.41 _{-3.60%}	23.57 _{+9.32%}	43.00 _{+5.01%}	59.98 _{+3.54%}
Dense	LoFTR [11]	21.61	40.03	55.82	25.68	45.86	62.60	20.36	39.44	57.16
	SGAM+LoFTR	22.05 _{+2.04%}	40.11 _{+0.20%}	56.65 _{+1.49%}	23.82 _{-7.24%}	44.19 _{-3.64%}	61.51 _{-1.74%}	21.94 _{+7.76%}	42.42 _{+2.48%}	57.42 _{+0.45%}
	MESA+LoFTR	23.41 _{+8.33%}	42.68 _{+6.62%}	57.68 _{+3.33%}	26.23 _{+2.14%}	46.06 _{+0.44%}	62.90 _{+0.48%}	22.55 _{+9.77%}	42.04 _{+6.59%}	58.34 _{+2.06%}
	DMESA+LoFTR	22.57 _{+4.44%}	40.67 _{+1.60%}	56.22 _{+0.72%}	24.37 _{-5.10%}	44.42 _{-3.14%}	61.34 _{-2.01%}	21.99 _{+8.01%}	40.53 _{+2.76%}	57.52 _{+0.63%}
Dense	DKM [13]	29.20	50.96	68.55	29.76	51.65	69.39	28.55	49.97	67.82
	SGAM+DKM	29.45 _{+0.86%}	51.74 _{+1.53%}	69.91 _{+1.98%}	30.33 _{+1.92%}	51.96 _{+0.60%}	69.54 _{+0.22%}	29.57 _{+3.57%}	50.86 _{+1.78%}	68.39 _{+0.84%}
	MESA+DKM	31.84 _{+9.04%}	53.07 _{+4.14%}	70.12 _{+2.29%}	32.14 _{+8.00%}	53.97 _{+4.49%}	71.02 _{+2.35%}	30.12 _{+5.50%}	51.03 _{+2.12%}	68.71 _{+1.31%}
DMESA+DKM	29.59 _{+1.34%}	51.21 _{+0.49%}	70.02 _{+2.14%}	30.77 _{+3.39%}	52.19 _{+1.05%}	69.52 _{+0.19%}	29.94 _{+4.87%}	51.35 _{+2.76%}	68.82 _{+1.47%}	

[†] The training size.

better matching performance. Note the aspect ratio conflict exists in this dataset (the training aspect ratio $\neq 1$). Thus we also evaluate the matching performance under the middle size of 640×480 . The choice of PM input resolution influences both computational requirements and matching accuracy, striking a balance between efficiency and precision in practice. By considering these various resolutions, we aim to comprehensively assess the practical value of our approach.

6.3.2 Results

The point matching results are summarised in Tab. 2. Subsequently, these results are analyzed with the categories of point matchers as the primary focus.

For the sparse matcher, SP+SG, as the baseline, we observe consistent and substantial accuracy improvements achieved by our methods across all three input sizes. Our methods surpass SGAM by a large margin. MESA exhibits the best overall performance, with DMESA also delivering impressive results. Particularly, MESA/DMESA+SP+SG gains better results with the small size of 480×480 than the large size of 640×640 (MESA on MMA@20: 56.87 vs. 56.29), achieving higher accuracy with less computational cost, proving its resolution robustness.

For three semi-dense matchers, the overfitting of training size is noticeable (cf. Sec. 3.3), as the results with the training size are remarkably surpass others. In the two square input sizes, our methods gain prominent improvements for all three matchers. In the training size, however, declines in precision are observed for MESA/DMESA+ASpan and MESA+LoFTR. This can partly attribute to sensitivity of aspect ratio in Transformer [37], as the training aspect ratio in ScanNet is slightly different from the one achieved by A2PM, which is inherent to original images. However, our methods still improve the results of QT and surpass SGAM. DMESA achieves generally better results than MESA due to its higher area matching accuracy (cf. Sec. 6.2). In all input sizes, the overall performance of DMESA is comparable to MESA. Considering its speed and flexibility, DMESA offers a better balance between efficiency and accuracy.

For the dense matcher, the issue of overfitting is relatively minor, thanks to the robustness of DKM. Our methods consistently improve the performance across all three input sizes, notably outperforming SGAM. Additionally, DMESA demonstrates superior performance in the small input size.

Comparing results across the baselines, the dense matcher achieves the best results at the expense of computational overhead. The sparse matcher enhanced by our methods achieves precision comparable to its semi-dense counterparts, at the small resolution of 480×480 (e.g., MESA+SP+SG on MMA@20: 56.87 vs. LoFTR: 55.86). This observation underscores the practical significance of our method, particularly in contexts with *constrained computational resources*.

6.4 Pose estimation

Pose estimation between images is one of the crucial geometric task subsequent to feature matching. Thus, we extensively evaluate the pose estimation precision of our methods in this section.

6.4.1 Experimental setup

In order to showcase the versatility of our methods, we conduct extensive experiments across four datasets encompassing both indoor and outdoor scenes. Specifically, we utilize two indoor datasets, ScanNet1500 and ETH3D [53], as well as two outdoor datasets, MegaDepth1500 [51] and YFCC [54]. ScanNet1500 and MegaDepth1500 each comprise 1500 image pairs suitable for evaluating camera pose estimation [12]. For ETH3D, we use the first 10 sequences to conduct experiments, with nearly 3K image pairs sampled from these sequences at a rate of 6, following [32]. Additionally, evaluations on YFCC have been conducted following [44], including 4000 outdoor image pairs. For each dataset, we choose a large size and a small size for complete evaluation. Moreover, for the datasets (ScanNet1500 and MegaDepth1500) used in baseline training, we further evaluate on the training size to investigate the overfitting issue.

Consistent with our prior experiments, we select five point matchers as the baselines. In the indoor scenes, we include

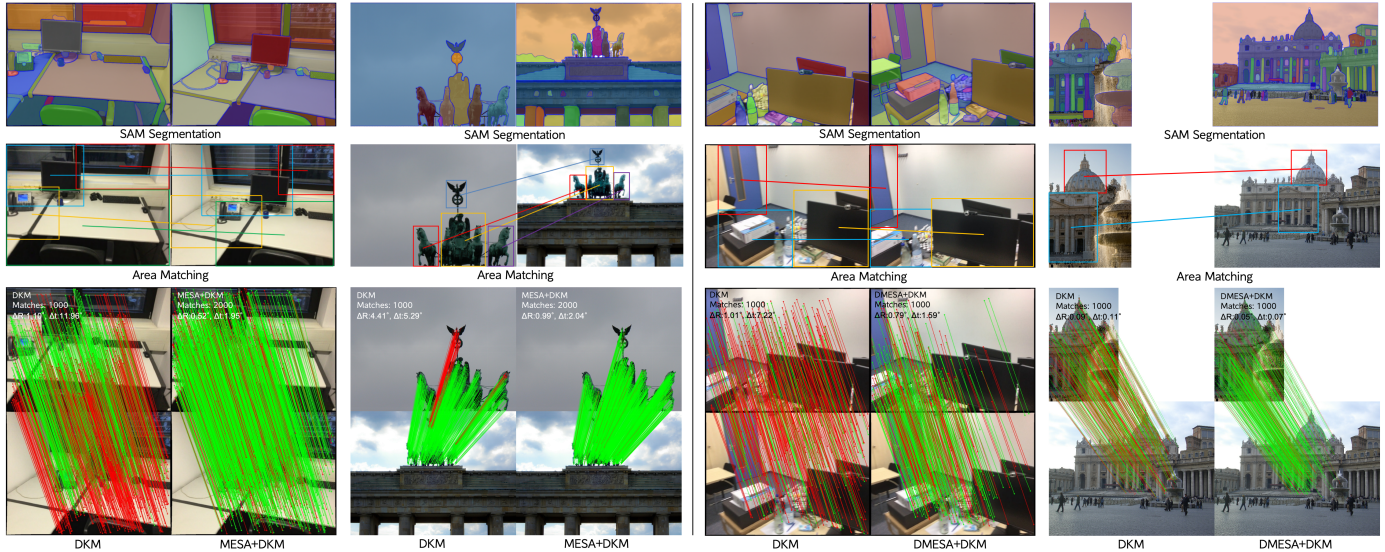


Fig. 7. **The qualitative results of our methods.** We provide qualitative results of MESA and DMESA on ScanNet1500 and MegaDepth1500. Our methods significantly improve the point matching and pose estimation performance of DKM, by attaining precise area matches.

TABLE 4

Pose Estimation on ETH3D. Relative gains are represented as subscripts. The **best**, **second** and **third** results are highlighted.

		Pose estimation AUC	AUC@5 \uparrow	AUC@10 \uparrow	AUC@20 \uparrow
640 \times 640	Sparse	SP [5]+SG [9]	19.09	32.89	46.59
		SGAM [18]+SP+SG	19.73 _{+3.35%}	33.14 _{+0.76%}	47.58 _{+2.12%}
		MESA+SP+SG	22.79 _{+19.38%}	36.43 _{+10.76%}	48.51 _{+4.12%}
		DMESA+SP+SG	20.30 _{+6.34%}	33.46 _{+1.73%}	46.56 _{-0.06%}
	Semi-Dense	ASpan [12]	16.92	31.06	45.5
		SGAM+ASpan	17.35 _{+2.54%}	31.88 _{+2.64%}	46.12 _{+1.36%}
		MESA+ASpan	22.31 _{+31.86%}	35.71 _{+14.97%}	50.07 _{+10.04%}
		DMESA+ASpan	18.73 _{+10.70%}	33.24 _{+7.02%}	47.83 _{+5.12%}
	Dense	LoFTR [11]	15.27	28.70	42.40
		SGAM+LoFTR	15.84 _{+3.73%}	29.34 _{+2.23%}	42.85 _{+1.06%}
		MESA+LoFTR	19.37 _{+26.85%}	32.82 _{+14.36%}	46.71 _{+10.17%}
		DMESA+LoFTR	15.99 _{+4.72%}	29.40 _{+2.44%}	43.00 _{+1.42%}
480 \times 480	Sparse	DKM	38.51	52.06	63.53
		SGAM+DKM	37.42 _{-2.83%}	51.53 _{-1.02%}	63.02 _{-0.80%}
		MESA+DKM	43.47 _{+12.88%}	55.32 _{+6.26%}	66.15 _{+4.12%}
		DMESA+DKM	38.27 _{-0.62%}	51.89 _{-0.33%}	63.31 _{-0.35%}
	Semi-Dense	SPSG	16.59	30.41	44.21
		SGAM+SPSG	17.31 _{+4.34%}	31.33 _{+3.03%}	44.78 _{+1.29%}
		MESA+SPSG	22.45 _{+35.32%}	35.68 _{+17.33%}	48.85 _{+10.50%}
		DMESA+SPSG	18.60 _{+12.12%}	32.39 _{+6.51%}	45.94 _{+3.91%}
	Dense	ASpan	8.61	18.94	32.49
		SGAM+ASpan	10.13 _{+17.65%}	19.35 _{+2.16%}	33.11 _{+1.91%}
		MESA+ASpan	15.57 _{+80.84%}	28.66 _{+51.32%}	42.74 _{+31.55%}
		DMESA+ASpan	13.91 _{+61.56%}	26.62 _{+40.55%}	40.82 _{+25.64%}
Semi-Dense	QT [21]	17.41	32.35	47.39	
	SGAM+QT	17.68 _{+1.55%}	32.93 _{+1.79%}	47.86 _{+0.99%}	
	MESA+QT	21.72 _{+24.76%}	36.77 _{+13.66%}	50.23 _{+5.99%}	
	DMESA+QT	19.29 _{+10.80%}	34.41 _{+6.37%}	49.10 _{+3.61%}	
Dense	LoFTR	9.12	19.34	32.79	
	SGAM+LoFTR	10.26 _{+12.50%}	19.97 _{+3.26%}	33.54 _{+2.29%}	
	MESA+LoFTR	15.19 _{+66.56%}	27.43 _{+41.83%}	40.22 _{+22.66%}	
	DMESA+LoFTR	12.26 _{+34.43%}	23.93 _{+23.73%}	37.51 _{+14.39%}	
Semi-Dense	DKM	36.25	49.45	60.34	
	SGAM+DKM	37.13 _{+2.43%}	49.85 _{+0.81%}	60.57 _{+0.38%}	
	MESA+DKM	39.98 _{+10.29%}	52.27 _{+5.70%}	62.74 _{+3.98%}	
	DMESA+DKM	36.31 _{+0.17%}	50.07 _{+1.25%}	61.57 _{+2.04%}	

SGAM as a comparison method. In the outdoor scenes, we contrast our methods with another overlap area matching technique, OETR [16]. The parameter $T_{E_{max}}$ of MESA is set as 0.35 for indoor scenes and 0.3 for outdoor scenes. Other parameters are fixed as described in Sec. 6.1.1.

Typically, the RANSAC [55] method is employed to filter outliers from point matches when deriving camera poses. However, fine-tuning RANSAC parameters can be cumbersome across diverse datasets. Therefore, in the following experiments, we employ MAGSAC++ [56] for outlier rejection, eliminating the necessity for RANSAC parameter adjustments and enhancing the reproducibility of our methods.

To facilitate straightforward result comparisons across the various datasets, we adopt a unified evaluation metric, specifically the standard pose estimation AUC, throughout all experiments. This metric represents the AUC of the pose error at the thresholds (AUC@5/10/20), where the pose error is defined as the maximum of angular error in rotation and translation.

6.4.2 Results on ScanNet1500

The pose estimation results on ScanNet1500 are reported in Tab. 3. Same as the point matching experiments, we evaluate the pose estimation accuracy across three PM input resolutions.

For the sparse matcher, our methods are able to enhance pose precision consistently and significantly across all resolutions. Notably, the precision gap between resolutions are minor. This indicates that our methods can offer stable improvements across various resolutions, given the point matcher itself is robust enough.

For the semi-dense matchers within A2PM framework, precision declines are observed at the training resolution, akin to the point matching experiments, except for MESA+LoFTR. This possibly results from the excessive area size adjustment at the resolution of 640 \times 480, which diminishes the advantages of A2PM. However, both MESA and DMESA do significantly improve pose precision at other square resolutions. As discussed in Sec. 3.3, this difference can be attributed to the overfitting issue inherent in Transformer [37]. To improve precision, fine-tuning of these matchers on square resolutions can be conducted, which sets a new SOTA on this dataset [24] and will be discussed later in Sec. 6.6.

TABLE 5
Pose Estimation on YFCC and MegaDepth1500. Relative gains are represented as subscripts. The **best**, **second** and **third** results are highlighted.

Pose estimation AUC	MegaDepth1500						YFCC						
	832 × 832 [†]		480 × 480		640 × 640		480 × 480						
	AUC@5 [†]	AUC@10 [†]	AUC@20 [†]	AUC@5 [†]	AUC@10 [†]	AUC@20 [†]	AUC@5 [†]	AUC@10 [†]	AUC@20 [†]	AUC@5 [†]	AUC@10 [†]	AUC@20 [†]	
Sparse	SP [5]+SG [9]	51.27	67.29	79.65	48.14	63.71	76.40	42.18	62.17	77.26	36.20	56.41	72.74
	OETR [16]+SP+SG	52.47 _{+2.34%}	68.35 _{+1.58%}	80.24 _{+0.74%}	51.22 _{+6.40%}	66.04 _{+3.66%}	78.43 _{+2.66%}	43.76 _{+3.75%}	64.11 _{+3.12%}	78.13 _{+1.13%}	36.77 _{+1.57%}	57.31 _{+1.60%}	73.52 _{+1.07%}
	MESA+SP+SG	56.27 _{+9.75%}	71.35 _{+6.03%}	82.11 _{+3.09%}	55.56 _{+15.41%}	70.89 _{+11.27%}	81.78 _{+7.04%}	45.25 _{+7.28%}	65.37 _{+5.15%}	79.78 _{+3.26%}	40.22 _{+11.10%}	59.79 _{+5.99%}	75.37 _{+3.62%}
	DMESA+SP+SG	57.69 _{+12.62%}	72.34 _{+7.50%}	83.10 _{+4.33%}	58.02 _{+20.52%}	71.77 _{+12.65%}	82.49 _{+9.77%}	42.57 _{+0.92%}	62.46 _{+0.47%}	77.47 _{+0.27%}	38.25 _{+5.66%}	58.12 _{+3.03%}	74.13 _{+1.94%}
Semi-Dense	ASpan [12]	62.45	75.96	85.45	48.66	64.47	76.89	46.67	65.96	79.65	41.65	61.39	76.48
	OETR+ASpan	63.38 _{+1.49%}	76.89 _{+1.22%}	86.30 _{+0.99%}	53.24 _{+9.41%}	66.37 _{+2.95%}	77.94 _{+1.37%}	47.37 _{+1.50%}	66.42 _{+0.70%}	79.97 _{+0.40%}	42.53 _{+2.11%}	62.27 _{+1.43%}	77.15 _{+0.88%}
	MESA+ASpan	64.56 _{+3.38%}	78.23 _{+2.99%}	87.11 _{+1.94%}	57.32 _{+17.80%}	70.96 _{+10.07%}	81.53 _{+6.03%}	48.78 _{+4.52%}	67.32 _{+2.06%}	81.55 _{+2.39%}	45.52 _{+9.29%}	61.97 _{+0.94%}	79.11 _{+3.44%}
	DMESA+ASpan	64.78 _{+3.73%}	78.00 _{+2.69%}	86.94 _{+1.74%}	61.76 _{+26.92%}	75.15 _{+16.57%}	84.37 _{+9.73%}	46.95 _{+0.60%}	66.08 _{+0.18%}	80.00 _{+0.44%}	43.32 _{+4.01%}	62.93 _{+2.51%}	77.85 _{+1.79%}
Dense	QT [21]	62.46	76.18	85.75	52.65	68.24	79.53	47.62	66.48	80.07	43.90	63.46	78.16
	OETR+QT	63.17 _{+1.14%}	77.32 _{+1.50%}	86.24 _{+0.57%}	53.72 _{+2.03%}	69.47 _{+1.80%}	80.69 _{+1.46%}	48.32 _{+1.47%}	67.17 _{+1.04%}	80.69 _{+0.77%}	44.62 _{+1.64%}	64.17 _{+1.12%}	78.88 _{+0.92%}
	MESA+QT	65.11 _{+4.24%}	78.32 _{+2.81%}	87.29 _{+1.80%}	57.28 _{+8.79%}	71.94 _{+5.42%}	83.16 _{+4.56%}	50.32 _{+5.67%}	68.31 _{+2.75%}	81.24 _{+1.46%}	47.21 _{+7.54%}	66.35 _{+4.55%}	80.13 _{+2.52%}
	DMESA+QT	65.01 _{+4.08%}	77.91 _{+2.27%}	86.74 _{+1.15%}	62.05 _{+17.85%}	75.69 _{+10.92%}	84.76 _{+6.58%}	48.32 _{+1.47%}	67.04 _{+0.84%}	80.45 _{+0.47%}	45.62 _{+3.92%}	64.84 _{+2.17%}	79.08 _{+1.18%}
Dense	LoFTR [11]	59.00	73.30	83.37	49.02	65.14	77.24	46.19	65.33	79.36	43.14	63.06	77.82
	OETR+LoFTR	60.47 _{+2.46%}	74.22 _{+1.26%}	84.28 _{+1.09%}	51.33 _{+4.71%}	66.71 _{+2.41%}	78.56 _{+1.71%}	46.67 _{+1.04%}	65.84 _{+0.78%}	79.93 _{+0.72%}	44.15 _{+2.34%}	64.17 _{+1.76%}	79.53 _{+2.20%}
	MESA+LoFTR	62.50 _{+5.90%}	75.33 _{+2.77%}	85.01 _{+1.97%}	55.17 _{+12.55%}	70.34 _{+7.98%}	81.18 _{+5.10%}	48.52 _{+5.04%}	67.31 _{+3.03%}	81.29 _{+2.43%}	46.23 _{+7.16%}	65.94 _{+4.57%}	80.21 _{+3.07%}
	DMESA+LoFTR	62.54 _{+5.96%}	76.06 _{+3.77%}	85.50 _{+2.55%}	60.23 _{+22.87%}	74.22 _{+13.94%}	83.82 _{+8.52%}	46.63 _{+0.95%}	65.56 _{+0.35%}	79.48 _{+0.15%}	44.60 _{+3.38%}	65.06 _{+3.17%}	78.74 _{+1.18%}
Dense	DKM [13]	62.37	75.80	85.14	61.70	75.24	84.49	51.07	68.75	81.24	50.95	68.73	81.33
	OETR+DKM	63.35 _{+1.57%}	76.23 _{+0.57%}	85.57 _{+0.51%}	63.18 _{+2.40%}	76.71 _{+1.95%}	85.12 _{+0.75%}	51.26 _{+0.37%}	69.31 _{+0.81%}	81.43 _{+0.24%}	50.97 _{+0.04%}	68.79 _{+0.09%}	81.24 _{-0.11%}
	MESA+DKM	65.21 _{+4.55%}	77.94 _{+2.82%}	86.93 _{+2.10%}	64.22 _{+4.08%}	77.52 _{+3.03%}	86.34 _{+2.19%}	52.13 _{+2.08%}	69.84 _{+1.59%}	81.95 _{+0.87%}	51.33 _{+0.75%}	68.97 _{+0.35%}	81.74 _{+0.50%}
	DMESA+DKM	65.48 _{+4.99%}	78.11 _{+3.05%}	86.63 _{+1.75%}	66.29 _{+7.44%}	78.50 _{+4.33%}	86.82 _{+2.76%}	51.60 _{+1.04%}	69.08 _{+0.48%}	81.50 _{+0.32%}	51.18 _{+0.45%}	68.79 _{+0.09%}	81.44 _{+0.14%}

[†]The training size.

For the dense matcher, although the best results are achieved at the training size, the disparity in accuracy across resolutions is relatively minor compared to the semi-dense matchers, indicating the resolution robustness of DKM. Hence, our methods consistently deliver prominent precision enhancement for DKM across all resolutions.

MESA+DKM yields the best results, which is consistent with the point matching experiments. SP+SG combined with our methods can surpass its semi-dense counterparts in the two square resolutions, e.g., AUC@20 of MESA+SP+SG: 61.49 vs. MESA+LoFTR: 57.68, with less computational cost. This proves the effectiveness of our methods. Overall, MESA performs better than DMESA by finding more area matches (higher ACR in Tab. 1 and see Fig. 7), as the pose estimation precision in this dataset is sensitive to the area diversity. However, at 480 × 480, this performance gap diminishes, particularly with DMESA+DKM surpassing MESA+DKM, demonstrating practical value of DMESA under limited computational overhead.

6.4.3 Results on ETH3D

The image pairs from ETH3D possess severe motion blur, light variation and textureless regions, leading to hard pose estimation. The results are summarised in Tab. 4. According to the resolution range of images in ETH3D [57], we choose 640 × 640 as the large size and 480 × 480 as the small one. To remove the resize distortion, we keep the original aspect ratio and use zero-padding to achieve square size, following [11], [44].

For the sparse matcher, our approaches lead to a substantial increase in accuracy. Particularly noteworthy is the performance of MESA+SPSG, which achieves a superior AUC@20 of 48.85 at 480 × 480 compared to 48.51 at 640 × 640. This serves as the evidence that our method enhances the resolution robustness of the point matcher.

For the three semi-dense matchers, our approach consistently improve the accuracy of point matching at two different resolutions. With the smaller resolution, the original point matchers experience significant performance degradation, which our method effectively mitigate by restoring much of the lost performance, attaining a relative improvement up to 80.84%.

For the dense matcher, the accuracy improvements brought by MESA remain impressive. DMESA relies on the coarse matching of ASpan for area matching. Due to the generalization issue of ASpan, its area matching accuracy falls short of that of MESA in this dataset. Moreover, dense DKM is more sensitive to the accuracy of area matching. Hence, a slight decrease in accuracy for DMESA+DKM at 640×640 is observed. However, at 480×480, DMESA still delivers performance improvements.

In summary, our approach considerably enhance the pose accuracy and resolution robustness of all point matchers on this dataset, surpassing SGAM by a large margin. Furthermore, DKM outperforms all other point matchers. Building upon this, MESA further enhance the accuracy of DKM, achieving performance comparable to the training set (ScanNet).

6.4.4 Results on MegaDepth1500

MegaDepth serves as the outdoor training dataset for our base-lines. In the MegaDepth1500 benchmark, we select a size of 832 × 832 as the large resolution, which is also used in training [11], [12], [21]. A small resolution (480×480) is also adopted for comparison. The resize distortion is avoided by shorter-side padding [9]. The results are reported in Tab. 5.

For the sparse matcher, our approaches yield stable and remarkable improvements in accuracy, surpassing OETR by a large margin. Furthermore, the precision gap between resolutions is notably reduced by MESA/DMESA, demonstrating the effectiveness of our method and their robustness to resolution variations.

For the semi-dense matchers, unlike the results on the indoor training dataset (ScanNet), our methods consistently and considerably improve pose accuracy. This can be interpreted as the training resolution on this dataset is square, aligning well with the A2PM framework. Thus, the precise AM achieved by our methods effectively reduce the matching redundancy on this dataset, ultimately increasing the performance of the semi-dense point matchers.

For the dense matcher, our methods also improve pose accuracy at both resolutions, setting a new SOTA on this benchmark. Considering the AM sensitivity of DKM, this proves the efficacy of MESA and DMESA.

TABLE 6
Visual Odometry on KITTI360. Relative gains are highlighted as subscripts. The **best**, **second** and **third** results are highlighted.

Visual Odometry	Seq. 00			Seq. 02			Seq. 05			Seq. 06			
	$R_{err} \downarrow$	$t_{err} \downarrow$	AUC@5 \uparrow	$R_{err} \downarrow$	$t_{err} \downarrow$	AUC@5 \uparrow	$R_{err} \downarrow$	$t_{err} \downarrow$	AUC@5 \uparrow	$R_{err} \downarrow$	$t_{err} \downarrow$	AUC@5 \uparrow	
Sparse	SP [5]+SG [9]	0.053	0.99	80.41	0.064	1.08	79.63	0.056	1.11	79.22	0.061	0.95	81.42
	SGAM [18]+SP+SG	0.036	0.89	82.98 _{+3.20%}	0.050	0.92	81.76 _{+2.67%}	0.042	0.96	81.57 _{+2.97%}	0.054	0.78	84.62 _{+3.93%}
	MESA+SP+SG	0.027	0.58	88.89 _{+10.55%}	0.041	0.82	87.33 _{+9.67%}	0.034	0.78	87.62 _{+10.60%}	0.037	0.62	88.24 _{+8.38%}
	DMESA+SP+SG	0.034	0.84	83.53 _{+3.88%}	0.046	0.89	82.80 _{+3.98%}	0.039	0.92	82.10 _{+3.64%}	0.041	0.75	85.28 _{+4.74%}
Semi-Dense	ASpan [12]	0.087	1.47	71.91	0.173	2.34	61.33	0.112	1.67	67.83	0.114	1.32	74.19
	SGAM+ASpan	0.054	1.32	76.22 _{+5.99%}	0.131	2.12	66.35 _{+8.19%}	0.083	1.43	73.46 _{+8.30%}	0.073	1.17	78.52 _{+5.84%}
	MESA+ASpan	0.068	1.17	78.25 _{+8.82%}	0.121	2.17	66.42 _{+8.30%}	0.078	1.39	76.72 _{+13.11%}	0.078	0.78	81.11 _{+9.33%}
	DMESA+ASpan	0.051	1.23	76.45 _{+6.31%}	0.134	2.10	66.08 _{+7.74%}	0.064	1.26	75.21 _{+10.88%}	0.062	1.01	80.36 _{+8.32%}
	QT [21]	0.131	2.97	58.10	0.164	3.84	55.26	0.152	3.60	53.42	0.153	2.87	60.06
	SGAM+QT	0.104	2.76	61.32 _{+5.54%}	0.131	3.42	58.23 _{+5.37%}	0.144	3.02	56.71 _{+6.16%}	0.110	2.41	63.21 _{+5.24%}
	MESA+QT	0.094	2.43	66.71 _{+14.82%}	0.113	3.14	66.21 _{+19.82%}	0.162	2.87	64.52 _{+20.78%}	0.123	2.33	71.22 _{+18.58%}
	DMESA+QT	0.080	2.49	61.10 _{+5.16%}	0.102	3.17	61.26 _{+10.86%}	0.151	2.59	60.50 _{+13.25%}	0.094	2.04	69.43 _{+15.60%}
Dense	LoFTR [11]	0.112	1.55	72.80	0.110	1.49	74.16	0.112	1.49	71.59	0.114	1.28	75.66
	SGAM+LoFTR	0.092	1.41	74.21 _{+1.94%}	0.093	1.40	76.22 _{+2.78%}	0.083	1.42	73.25 _{+2.32%}	0.095	1.22	77.26 _{+2.11%}
	MESA+LoFTR	0.083	1.32	75.33 _{+3.48%}	0.087	1.44	75.63 _{+1.98%}	0.076	1.35	75.24 _{+5.10%}	0.088	1.21	79.44 _{+5.00%}
	DMESA+LoFTR	0.057	1.22	78.50 _{+7.83%}	0.070	1.18	78.66 _{+6.07%}	0.064	1.09	78.46 _{+9.60%}	0.061	0.95	81.92 _{+8.27%}
Dense	DKM [13]	0.027	0.30	94.08	0.099	0.49	91.52	0.039	0.43	91.40	0.034	0.38	92.31
	SGAM+DKM	0.022	0.25	95.32 _{+1.32%}	0.046	0.41	92.34 _{+0.90%}	0.026	0.31	92.68 _{+1.40%}	0.027	0.34	93.67 _{+1.47%}
	MESA+DKM	0.018	0.20	96.13 _{+2.18%}	0.027	0.33	94.32 _{+3.06%}	0.022	0.25	95.18 _{+4.14%}	0.022	0.26	95.31 _{+3.25%}
	DMESA+DKM	0.022	0.29	94.13 _{+0.05%}	0.034	0.44	91.94 _{+0.46%}	0.028	0.41	92.34 _{+1.03%}	0.026	0.35	93.05 _{+0.80%}

Overall, on this dataset, our method significantly surpasses the previous SOTA (OETR). Particularly noteworthy is the outstanding performance of DMESA compared to MESA, demonstrating superior results in terms of both accuracy and efficiency. This can be interpreted as MegaDepth being the training set for the patch matching used in DMESA as the basis of AM. Thus the accurate AM of DMESA contributes to its high pose precision. Notably, DMESA+DKM achieves superior results with the small resolution compared to the large one (AUC@5: 66.29 of 480×480 vs. 65.48 of 832 × 832), impressively leading to numerous reductions in computational costs.

6.4.5 Results on YFCC

As per [15], [36], the longer sides of YFCC images are typically shorter than 640. Therefore, in this experiment, we choose 640 × 640 as the larger resolution and 480 × 480 as the smaller one. To prevent aspect ratio distortions, we apply shorter-side padding during resizing [9]. The results are reported in Tab. 5.

For the sparse point matcher, MESA brings about the most noteworthy improvement in accuracy, with a more pronounced enhancement at 480 × 480. The performance improvement of DMESA is not as strong as OETR at 640 × 640, which may be attributed to the generalization issues of the coarse matcher on which DMESA relies. However, at the smaller resolution, DMESA outperforms OETR, highlighting the robustness of our method to resolution variations.

For the semi-dense matchers, MESA also leads to the most prominent improvement for all matchers at both resolutions. DMESA sacrifices some accuracy but in return gains greater speed and improved flexibility. It also performs better at the smaller resolution, surpassing OETR.

For the dense matcher, our approaches demonstrate consistent accuracy improvements, albeit relatively limited. This may be attributed to the increased difficulty in area matching caused by the abundance of repetitive textures in the YFCC dataset, as the DKM is sensitive to AM accuracy.

Overall, on this dataset, MESA shows the best performance and demonstrates superior generalization. Both of our approaches generally outperform OETR, proving their effectiveness.

6.5 Visual Odometry

To further evaluate the performance of our methods in downstream tasks, we conducted experiments on visual odometry, using the KITTI360 dataset, which densely estimates the camera motion in the driving scene.

6.5.1 Experimental setup

According to the static scene assumption [1] of our baselines, we select four sequences from the dataset that contain a small number of moving objects, each comprising 3000 images. The parameter $T_{E_{max}}$ of MESA is set as 0.25. The input image size is 640 × 640. We utilize the same baselines as in other experiments, which are trained on ScanNet [50]. MAGSAC++ is used to estimate poses from the correspondences. Following [58], we report the relative pose errors (RPE), including the rotational error (R_{err}) and translation error (t_{err}). Also, the pose estimation AUC@5 is reported for better comparisons.

6.5.2 Results

The results are presented in Tab. 6. For the sparse matcher, MESA and DMESA both obtain notable and consistent improvement across all sequences, surpassing SGAM, validating the effectiveness of our methods.

For the semi-dense matchers, the performance improvement brought by our methods is remarkable. MESA and DMESA respectively yield performance boosts of up to 20.78% and 15.60%. It is worth noting that when employing LoFTR, DMESA outperforms MESA across all sequences with increased efficiency, making it a more practical choice in this scene.

For the dense matcher, our methods further enhance its accuracy, achieving the best results on this dataset. While the performance of DMESA is inferior to SGAM, it still provides an enhancement for DKM. This possibly is caused by the AM sensitivity of DKM and generalization challenge of DMESA.

In this experiment, our method has demonstrated the ability to enhance the accuracy of visual odometry for all point matchers. Notably, when integrated with our approach, SP+SG exhibits substantial improvements. These outcomes surpass semi-dense

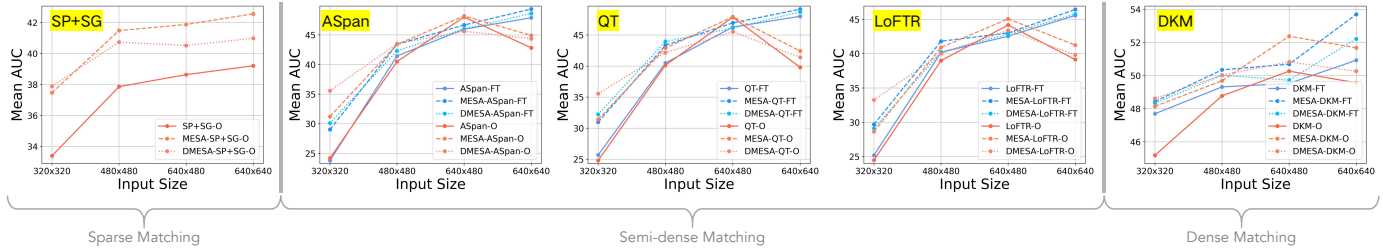


Fig. 8. Experiment Results about Input Size and Model Fine-Tuning. The figure illustrates pose estimation experiments with five point matchers on ScanNet1500, displaying a line graph of pose accuracy concerning input sizes. Two types of dashed lines represent the results of MESA and DMESA. The orange lines indicate the outcomes of the original models trained on the resolution of 640×480 , while the blue lines represent the results of models fine-tuned on the resolution of 640×640 .

matchers by a considerable margin, even approaching the performance level of dense matching. Given the efficiency advantage of sparse matching over dense/semi-dense matching, this evidently emphasizes the practical value of our methods.

6.6 Study of PM Resolution and Model Fine-tuning

In addition to the investigation of the PM resolution conducted in the aforementioned experiments, in this section, we delved more deeply into the impact of image resolution on pose estimation accuracy on ScanNet1500. This includes exploring a broader range of resolutions and conducting comparative experiments incorporating factors of model fine-tuning tailored to the specific resolution.

6.6.1 Experimental setup

On ScanNet1500, we select four sets of *input sizes* (i.e. resolution), including three square sizes ranging from small to large ($[320^2, 480^2, 640^2]$) and one training resolution of 640×480 . The same five point matchers, covering three types, are utilized, consistent with the previous experiments. With the exception of SP+SG, which does not encounter any overfitting issue in previous experiments, we fine-tune the other four point matchers at 640×640 , obtaining fine-tuned models identified by a ‘-FT’ suffix. The original models are labeled with an ‘-O’ suffix. We evaluate the performance of different methods using the average of pose estimation AUC@5/10/20, referred to as *Mean AUC*.

6.6.2 Results

The results are depicted in Fig. 8. *For the sparse matcher*, our methods not only significantly improve accuracy but also greatly reduce the gap in accuracy across different resolutions, demonstrating the efficacy of our methods and their enhancement of resolution robustness. The results of DMESA are particularly strong at 320×320 , surpassing even those of MESA.

For semi-dense matchers, we observe that the original models exhibit a consistent performance peak at the training size, indicating overfitting to this specific resolution and a high sensitivity to resolution variations. Consequently, our methods do not show an advantage over the original model at the training size (except for MESA+LoFTR) but do improve accuracy at other sizes. For the fine-tuned models, our approaches enhance accuracy across all resolutions, surpassing the performance of original models at the training size. We also note a decrease in performance on the training size for the fine-tuned models, indicating that fine-tuning may not be the optimal solution for resolution sensitivity. DMESA still demonstrates outstanding performance at the smaller resolution.

For the dense matcher, although the performance peak still exists, the original model exhibits much less sensitivity to resolution compared to semi-dense methods (note the scale of the vertical axis). Therefore, our methods significantly improve accuracy for the original model across all sizes. After fine-tuning, the performance of MESA and DMESA is further enhanced. DMESA continues to excel at the smaller resolution, consistent with its emphasis on efficiency.

Overall, our methods boost the accuracy of point matchers and enhance their robustness to resolution variations. Model fine-tuning is also effective to address the overfitting issue. Notably, MESA demonstrates superior accuracy at higher resolutions, whereas DMESA stands out at lower resolutions. Both approaches are viable for practical implementation based on specific computational resource constraints.

6.7 Study of Cross-Domain Generalization

Given the broad range of application scenarios for the feature matching task, the ability to generalize across domains is a crucial performance metric for feature matching methods. Therefore, in this section, we construct experiments to evaluate the cross-domain generalization of our methods.

6.7.1 Experimental setup

To establish the cross-domain matching task, we employ models trained in the outdoor dataset (MegaDepth), including both the point matching models and learning models of MESA/DMESA, to perform feature matching on indoor images (ScanNet1500). The baseline selection, input size configuration, and method parameter settings for this experiment are kept consistent with other experiments on the ScanNet1500 dataset (cf. Sec. 6.4).

6.7.2 Results

We present the results in Tab. 7. *For the sparse matcher*, our methods result in an overall increase in accuracy, narrowing the gap with in-domain precision, showcasing the prominent generalization. It is noteworthy that our methods achieve the best results at the smallest resolution of 480×480 , proving the resolution robustness of our methods. This also means our methods can attain better accuracy with less computational cost, which matters in applications with limited computation budget.

For semi-dense point matchers, the accuracy drop on training sizes observed in in-domain experiments is eliminated, replaced by an overall performance improvement with our methods. This indicates that our approaches can significantly enhance the generalization of semi-dense point matchers. Moreover, our methods

TABLE 7

Cross-Domain Evaluation of Pose Estimation. We apply the learning models (including point matching models in baselines and area matching models in MESA and DMESA) trained on the outdoor scene (MegaDepth) to estimate camera poses in the indoor scene (ScanNet). Relative gains are highlighted as subscripts. The **best**, **second** and **third** results are highlighted.

Pose estimation AUC	640 × 640			640 × 480			480 × 480			
	AUC@5↑	AUC@10↑	AUC@20↑	AUC@5↑	AUC@10↑	AUC@20↑	AUC@5↑	AUC@10↑	AUC@20↑	
Sparse	SP [5]+SG [9]	20.46	38.27	54.92	20.08	38.03	55.02	18.84	36.61	53.49
	MESA+SP+SG	22.34 _{+9.19%}	39.95 _{+4.39%}	56.88 _{+3.57%}	22.43 _{+11.70%}	40.12 _{+5.50%}	57.04 _{+3.67%}	22.47 _{+19.27%}	41.23 _{+12.62%}	57.89 _{+8.23%}
	DMESA+SP+SG	20.67 _{+1.03%}	38.27 _{+0.00%}	54.56 _{-0.66%}	20.60 _{+2.59%}	38.37 _{+0.89%}	55.28 _{+0.47%}	20.79 _{+10.35%}	38.63 _{+5.52%}	55.25 _{+3.29%}
Semi-Dense	ASpan [12]	21.99	40.21	56.87	24.11	43.61	60.22	22.82	41.78	58.32
	MESA+ASpan	24.21 _{+10.10%}	43.77 _{+8.85%}	60.08 _{+5.64%}	25.31 _{+4.98%}	46.18 _{+5.89%}	62.04 _{+3.02%}	24.22 _{+6.13%}	44.16 _{+5.70%}	60.98 _{+4.56%}
	DMESA+ASpan	22.91 _{+4.18%}	41.40 _{+2.96%}	57.44 _{+1.00%}	23.81 _{-1.24%}	43.46 _{-0.34%}	60.50 _{+0.46%}	23.96 _{+5.00%}	43.06 _{+3.06%}	59.43 _{+1.90%}
	QT [21]	22.40	40.10	56.90	22.25	41.51	58.51	21.77	40.31	57.02
	MESA+QT	24.64 _{+10.00%}	43.91 _{+9.50%}	61.45 _{+8.00%}	24.32 _{+9.30%}	43.98 _{+5.95%}	60.99 _{+4.24%}	24.73 _{+13.60%}	44.15 _{+9.53%}	60.84 _{+6.70%}
	DMESA+QT	23.46 _{+4.73%}	41.98 _{+4.69%}	58.51 _{+2.83%}	23.06 _{+3.64%}	42.05 _{+1.30%}	59.08 _{+0.97%}	22.68 _{+4.18%}	41.82 _{+3.75%}	58.65 _{+2.86%}
	LoFTR [11]	19.79	36.91	52.63	20.94	38.68	54.61	19.82	37.59	53.28
	MESA+LoFTR	21.34 _{+7.83%}	39.23 _{+6.29%}	55.12 _{+4.73%}	22.31 _{+6.54%}	40.34 _{+4.29%}	57.12 _{+4.60%}	21.56 _{+8.78%}	40.07 _{+6.60%}	57.33 _{+7.60%}
	DMESA+LoFTR	20.99 _{+6.06%}	38.51 _{+4.33%}	54.23 _{+3.04%}	21.11 _{+0.81%}	39.14 _{+1.19%}	55.29 _{+1.25%}	21.17 _{+6.81%}	39.49 _{+5.05%}	55.50 _{+4.17%}
Dense	DKM [13]	25.67	46.01	63.05	27.00	47.42	64.59	25.75	45.71	62.96
	MESA+DKM	28.91 _{+12.62%}	48.77 _{+6.00%}	65.18 _{+3.38%}	28.89 _{+7.00%}	49.34 _{+4.05%}	66.32 _{+2.68%}	28.12 _{+9.23%}	48.31 _{+5.00%}	65.49 _{+3.87%}
	DMESA+DKM	25.92 _{+0.97%}	46.33 _{+0.70%}	62.84 _{-0.33%}	27.14 _{+0.52%}	47.39 _{-0.06%}	64.70 _{+0.17%}	26.11 _{+1.40%}	46.09 _{+0.83%}	63.33 _{+0.59%}

TABLE 8

Ablation study of MESA. Four variants of MESA+ASpan are evaluated for area matching and pose estimation on the ScanNet1500 to demonstrate the importance of various components.

Method	AOR ↑	AMP@0.6 ↑	PoseAUC@5 ↑	ACR ↑
MESA+ASpan (Ours)	72.75	89.09	27.50	95.80
w/ CSD	69.23	84.21	26.78	87.33
w/ <i>DesSim</i> . [44]	63.71	62.91	26.05	80.11
w/ <i>SEEMSeg</i> . [59]	70.58	85.52	26.18	72.51
w/ arg min E_{self}	70.98	87.56	26.96	91.64

reduce the accuracy gap between different sizes, showcasing their resolution robustness.

For the dense matcher, our methods lead to a remarkable increase in accuracy. Particularly at the small size of 480 × 480, MESA+DKM reaches the precision level of in-domain performance (cf. Tab. 3), demonstrating the enhancement of our method on the cross-domain generalization.

In the experiments, MESA showcases better generalization in contrast to DMESA, as the pre-trained coarse matcher in DMESA suffers from the domain gap. Nonetheless, leveraging the benefits of A2PM and the remarkable versatility of SAM, DMESA still contributes to improving the generalization of point matchers.

6.8 Ablation Study

6.8.1 Understanding MESA

To evaluate the effectiveness of our design, we conduct a comprehensive ablation study for components of MESA. In this experiments, we use the MESA+ASpan as the baseline. The input size of the point matching is 640 × 640 and the model of ASpanFormer is fine-tuned in 640 × 640 as well.

Area Graph Construction. To justify the AG of MESA, we adopt a naive approach to match areas, which is comparing area similarity densely (CSD). In particular, we first select areas with proper size from all SAM areas of two images. The similarity of each area to all areas in the other images is then calculated and area matches with the greatest similarity is obtained. The comparison results are summarised in Tab. 8. As AG can generate more proper areas for matching, MESA w/ CSD gets less area

matches. Thus, the area and point matching performance is also decreased by CSD. Moreover, CSD results in a significant increase in time of area matching (nearly ×10 slower than MESA), due to its inefficient dense comparison.

Area Similarity Calculation. In contrast to our classification formulation for area similarity calculation, another straightforward method [44] involves calculating the distance between learning descriptors of areas. Thus, we replace our learning similarity with descriptor similarity in [44] (*DesSim*) and conduct experiments in ScanNet to investigate the impact. The results are summarized in Tab. 8, including the area number per image, area matching and pose estimation performance. Overall, the performance of *DesSim* experiences a noticeable decline, due to poor area matching precision, indicating the effectiveness and importance of proposed learning similarity calculation.

Image Segmentation Source. We rely on SAM to achieve areas with implicit semantic, whose outstanding segmentation precision and versatility contribute to our leading matching performance. However, areas can also be obtained from other segmentation methods. Therefore, to measure the impact of different segmentation sources, we exchange the segmentation input from SAM [14] with that from SEEM [59] (*SEEMSeg.*) and evaluate the performances. In Tab. 8, MESA with *SEEMSeg.* gets a slight precision decline and fewer areas compared with SAM, leading to decreased pose estimation results. These results indicates that the advanced segmentation favors our methods. Notably, MESA with *SEEMSeg.* also achieves a slight improvement for ASpan, proving the effectiveness of MESA.

Global Energy Refinement. After *Graph Cut*, the proposed global matching energy for the final area matching refinement considers structures of both AGs of the input image pair. To show the importance of this dual-consideration, we replace the global energy with naive E_{self} in Eq. (13) (arg min E_{self}) and evaluate the performance. In Tab. 8, the refinement relying on E_{self} produces decreased area matching precision and a subsequent decline in pose estimation performance, due to inaccurate area matches especially under repetitiveness. The qualitative results shown in Fig. 9 further indicate the better robustness of global energy under repetitiveness due to dual graph structure capture.

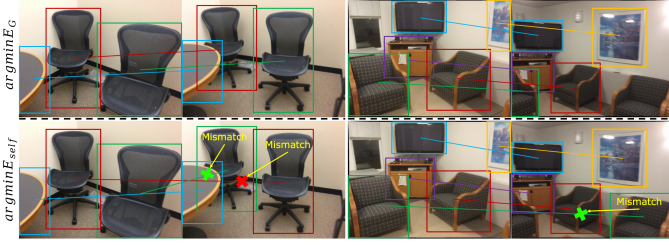


Fig. 9. **The qualitative comparison of Global Energy Refinement.** As AG structures of both images are considered by E_G , objects with the same apparent can be distinguished according to their neighbors, which are mismatched by $\arg \min E_{self}$, revealing the robustness of $\arg \min E_G$ under repetitive patterns.

TABLE 9

Ablation study of DMESA. We show area matching and pose estimation performance of SP+SG+DMESA on ScanNet1500 w.r.t two parameters of DMESA. The parameters we applied are **highlighted**.

		AOR \uparrow	AMP@0.6 \uparrow	Pose AUC@5 \uparrow	ACR \uparrow
T_c	$f(1/8)^\dagger$	79.11	88.02	22.13	77.12
	$f(1/2)^\dagger$	79.26	87.54	21.68	78.02
	$f(1)^\dagger$	78.13	86.45	22.19	79.44
	$f(2)^\dagger$	77.41	84.13	21.56	80.22
	$f(4)^\dagger$	75.26	80.55	21.28	81.39
S_{EM}	0	75.82	85.97	21.68	78.84
	1	79.38	86.52	21.37	76.53
	3	78.13	86.45	22.19	79.44
	5	77.30	86.59	21.57	81.13
	7	76.14	85.74	21.69	83.66

$$\dagger f(x) = \frac{1}{2\pi} e^{-x}$$

6.8.2 Understanding DMESA

In contrast to the complex parameter settings of MESA, DMESA involves just two parameters necessitating configuration. One parameter is the confidence threshold T_c for area extraction from the heatmap; while the other, *i.e.* the EM algorithm step number S_{EM} , regulates the degree of fusion in the results of the two matching directions. In this section, we perform ablation study on the two parameters using SP+SG as the point matcher on ScanNet1500, assessing both area matching and pose estimation precision. Given the orthogonal nature of two parameters, during experiments focusing on one parameter, we retain the other at its default setting ($T_c = \frac{1}{2\pi} e^{-1}$, $S_{EM} = 3$).

Confidence Threshold. On the AM heatmap, only pixels with confidence exceeding the T_c contribute to area matching. These confidences are determined by a GMM from the patch matches. Hence, we use the standard Gaussian distribution ($\mathcal{N}(\mathbf{x}|0, I) = \frac{1}{2\pi} \exp(-\|\mathbf{x}\|^2/2)$) as a reference to set this threshold T_c . Specifically, we choose $\|\mathbf{x}\| = [1/2, 1, \sqrt{2}, 2, 2\sqrt{2}]$, resulting in corresponding confidence thresholds of: $[\frac{1}{2\pi} e^{-1/8}, \frac{1}{2\pi} e^{-1/2}, \frac{1}{2\pi} e^{-1}, \frac{1}{2\pi} e^{-2}, \frac{1}{2\pi} e^{-4}]$. The results are reported in Tab. 9. We observe that AM accuracy increases with T_c . However, as the coverage of areas (ACR) in the image decreases at the same time, there may be a loss of matching points, harmful to pose estimation accuracy. Therefore, we select $T_c = \frac{1}{2\pi} e^{-1}$ as the threshold, striking a balance between AM accuracy and coverage, thereby achieving the best pose estimation accuracy.

TABLE 10

Time Consumption Comparison. The average time cost of area matching per image utilizing different methods is summarised. The experiment is conducted on 500 image pairs sampled from YFCC.

Method	Step	Time(ms)
MESA	AG Construction	384.22
	Similarity Calculation	2953.17
	Graph Cut	3.24
	Energy Minimization	6.15
	Total	3346.78
DMESA	AG Construction	378.13
	Coarse Matching	118.35
	Patch Confidence Rendering	84.56
	EM Refinement	125.39
	Total	706.43
SGAM [18]	Total	693.87
OETR [16]	Total	653.74

Step number of EM. DMESA merges the results of two different matching directions using a finite-step EM algorithm, thus improving the area matching through cycle consistency. Hence, the number of EM algorithm steps should be kept moderate; excessively low or high step counts may bias the refined results towards one matching direction rather than achieving a consistent outcome between the two. We experimented with values of $S_{EM} = [0, 1, 3, 5, 7]$, and the results are presented in Tab. 9. It is evident that the step count influences both the area matching accuracy (AOR) and coverage (ACR), thus resulting nonlinear variations in pose estimation precision. A moderate setting of $S_{EM} = 3$ can yield the best pose estimation accuracy. We also provide qualitative results about the S_{EM} in Fig. 10, further justifying the efficacy of the moderate setting.

6.9 Running Time Comparison

In this section, the average time consumption of AM methods on each image pair is recorded, to compare the efficiency.

6.9.1 Experimental setup

To facilitate comparison with other methods, we randomly sampled 500 images from the YFCC dataset with a resolution of 480×480 for constructing the experiment. This experiment is conducted on an Intel Xeon Silver 4314 CPU and a GeForce RTX 4090 GPU. Our comparative methods include SGAM, which establishes area matches grounded on explicit semantic, and OETR, which focuses on establishing matches of co-visible areas. In addition, we record the time consumption of the individual modules for both MESA and DMESA.

6.9.2 Results

The results are summarised in Tab. 10. From the table, it is evident that MESA incurs the longest time consumption, primarily due to the intensive computation involved in assessing area similarities. This can be attributed to the sparse matching framework of MESA, which leads to numerous similarity calculations among candidates, as described in Sec. 5. Therefore, DMESA adopts a dense matching framework, effectively reducing the number of area similarity calculations. By incorporating a coarse matching stage of an off-the-shelf point matcher, the cost of single area matching is further reduced. Ultimately, DMESA achieves a speed approximately 5 times faster than MESA while maintaining competitive accuracy. Furthermore, the speed of DMESA aligns closely with that of the other two SOTA methods, affirming its practical utility.

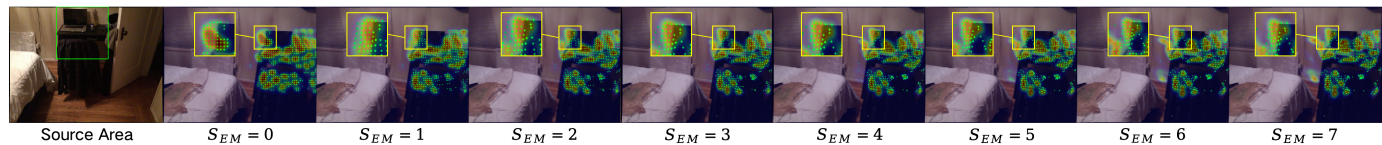


Fig. 10. **The qualitative results of finite-step EM refinement of DMESA.** We present the source area along with its corresponding patch matches in the target image across various EM step numbers (S_{EM}). The green dots are patch centers and the distributions of GMM are visualized as well. With the increase of S_{EM} , the patches become clustered into image regions with distinct features (e.g., the upper-left corner of the laptop in the bottom). These regions exhibit high confidence in both matching directions, thereby enhancing overall accuracy. Additionally, it is evident that an excessively large S_{EM} does not contribute to patch refinement, as the patches are already stabilized in the initial stages.

7 CONCLUSION

We introduce MESA and DMESA to reduce redundancy in feature matching by leveraging the general image understanding capability of SAM. While both methods focus on establishing area matching from SAM results, MESA follows a sparse framework, whereas DMESA adopts a dense fashion. Specifically, we first propose a novel Area Graph (AG) to model the global context of image areas. Based on this graph, candidate areas with prominent semantics can be identified from images. Subsequently, MESA minimizes energy on the graph to match these areas, leveraging graphical models derived from AG. While MESA is precise, its sparse nature poses efficiency challenges. To overcome this limitation, DMESA is proposed as a dense area matching method. DMESA deduces area matches from off-the-shelf patch matches, which are modeled through the GMM. Then dense matching heatmaps for source areas are generated in the target image to achieve area matches. To refine the accuracy of coarse matching, DMESA further introduces cycle consistency and employs a finite-step EM algorithm. Our methods enable integration with PM baselines belonging to sparse, semi-dense and dense frameworks. In extensive experiments, both MESA and DMESA consistently and significantly increase the performance for five baselines across five indoor and outdoor datasets. DMESA demonstrates a nearly fivefold speed improvement over MESA while maintaining competitive accuracy, offering a superior accuracy/speed trade-off. Besides, our methods substantially improve the robustness against variations in data domain and input resolution, benefiting the downstream tasks.

REFERENCES

- [1] C. Campos, R. Elvira, J. J. G. Rodríguez, J. M. Montiel, and J. D. Tardós, “Orb-slam3: An accurate open-source library for visual, visual–inertial, and multimap slam,” *IEEE Transactions on Robotics*, 2021. **1, 13**
- [2] J. L. Schonberger and J.-M. Frahm, “Structure-from-motion revisited,” in *Proceedings of the IEEE conference on computer vision and pattern recognition*, 2016, pp. 4104–4113. **1**
- [3] P.-E. Sarlin, A. Unagar, M. Larsson, H. Germain, C. Toft, V. Larsson, M. Pollefeys, V. Lepetit, L. Hammarstrand, F. Kahl *et al.*, “Back to the feature: Learning robust camera localization from pixels to pose,” in *Proceedings of the IEEE/CVF Conference on Computer Vision and Pattern Recognition*, 2021, pp. 3247–3257. **1**
- [4] J. Ma, X. Jiang, A. Fan, J. Jiang, and J. Yan, “Image matching from hand-crafted to deep features: A survey,” *International Journal of Computer Vision*, vol. 129, no. 1, pp. 23–79, 2021. **1**
- [5] D. DeTone, T. Malisiewicz, and A. Rabinovich, “Superpoint: Self-supervised interest point detection and description,” *Proceedings of the IEEE conference on computer vision and pattern recognition workshops*, pp. 224–236, 2018. **1, 3, 9, 10, 11, 12, 13, 15**
- [6] Z. Luo, L. Zhou, X. Bai, H. Chen, J. Zhang, Y. Yao, S. Li, T. Fang, and L. Quan, “Aslfeat: Learning local features of accurate shape and localization,” *Computer Vision and Pattern Recognition (CVPR)*, 2020. **1**
- [7] J. Revaud, C. De Souza, M. Humenberger, and P. Weinzaepfel, “R2d2: Reliable and repeatable detector and descriptor,” *Advances in neural information processing systems*, vol. 32, 2019. **1, 3**
- [8] M. Dusmanu, I. Rocco, T. Pajdla, M. Pollefeys, J. Sivic, A. Torii, and T. Sattler, “D2-net: A trainable cnn for joint description and detection of local features,” *Proceedings of the IEEE/cvf conference on computer vision and pattern recognition*, pp. 8092–8101, 2019. **1, 3, 9**
- [9] P.-E. Sarlin, D. DeTone, T. Malisiewicz, and A. Rabinovich, “Superglue: Learning feature matching with graph neural networks,” *Proceedings of the IEEE/CVF Conference on Computer Vision and Pattern Recognition (CVPR)*, June 2020. **1, 3, 8, 9, 10, 11, 12, 13, 15**
- [10] P. Lindenberger, P.-E. Sarlin, and M. Pollefeys, “LightGlue: Local feature matching at light speed,” *ICCV*, 2023. **1**
- [11] J. Sun, Z. Shen, Y. Wang, H. Bao, and X. Zhou, “LoFTR: Detector-free local feature matching with transformers,” *CVPR*, 2021. **1, 2, 3, 6, 9, 10, 11, 12, 13, 15, 19**
- [12] H. Chen, Z. Luo, L. Zhou, Y. Tian, M. Zhen, T. Fang, D. McKinnon, Y. Tsin, and L. Quan, “Aspanformer: Detector-free image matching with adaptive span transformer,” *ECCV*, pp. 20–36, 2022. **1, 2, 3, 6, 7, 8, 9, 10, 11, 12, 13, 15**
- [13] J. Edstedt, I. Athanasiadis, M. Wadenbäck, and M. Felsberg, “DKM: Dense kernelized feature matching for geometry estimation,” *CVPR*, 2023. **1, 2, 3, 9, 10, 12, 13, 15**
- [14] A. Kirillov, E. Mintun, N. Ravi, H. Mao, C. Rolland, L. Gustafson, T. Xiao, S. Whitehead, A. C. Berg, W.-Y. Lo, P. Dollár, and R. Girshick, “Segment anything,” *ICCV*, 2023. **1, 5, 15**
- [15] D. Huang, Y. Chen, Y. Liu, J. Liu, S. Xu, W. Wu, Y. Ding, F. Tang, and C. Wang, “Adaptive assignment for geometry aware local feature matching,” *CVPR*, 2023. **1, 13**
- [16] Y. Chen and *et al.*, “Guide local feature matching by overlap estimation,” *AAAI*, vol. 36, no. 1, pp. 365–373, 2022. **1, 3, 11, 12, 16**
- [17] K. T. Giang, S. Song, and S. Jo, “Topicfm: Robust and interpretable topic-assisted feature matching,” *AAAI*, vol. 37, no. 2, pp. 2447–2455, 2023. **1, 3**
- [18] Y. Zhang, X. Zhao, and D. Qian, “Searching from area to point: A hierarchical framework for semantic-geometric combined feature matching,” *arXiv*, 2023. **1, 2, 3, 4, 8, 9, 10, 11, 13, 16, 21**
- [19] J. Ma and B. Wang, “Segment anything in medical images,” *arXiv preprint arXiv:2304.12306*, 2023. **2**
- [20] T. Yu, R. Feng, R. Feng, J. Liu, X. Jin, W. Zeng, and Z. Chen, “Inpaint anything: Segment anything meets image inpainting,” *arXiv preprint arXiv:2304.06790*, 2023. **2**
- [21] S. Tang, J. Zhang, S. Zhu, and P. Tan, “Quadtree attention for vision transformers,” *ICLR*, 2022. **2, 3, 9, 10, 11, 12, 13, 15, 19**
- [22] V. Kolmogorov and R. Zabini, “What energy functions can be minimized via graph cuts?” *IEEE transactions on pattern analysis and machine intelligence*, vol. 26, no. 2, pp. 147–159, 2004. **2, 6**
- [23] P. Gleize, W. Wang, and M. Feiszli, “Silk—simple learned keypoints,” *ICCV*, 2023. **2, 7, 8**
- [24] Y. Zhang and X. Zhao, “Mesa: Matching everything by segmenting anything,” in *IEEE Conference on Computer Vision and Pattern Recognition (CVPR)*, 2024. **2, 11**
- [25] D. G. Lowe, “Distinctive image features from scale-invariant keypoints,” *International journal of computer vision*, vol. 60, no. 2, pp. 91–110, 2004. **3**
- [26] E. Rublee, V. Rabaud, K. Konolige, and G. Bradski, “Orb: An efficient alternative to sift or surf,” *2011 International conference on computer vision*, pp. 2564–2571, 2011. **3**
- [27] A. Barroso-Laguna, E. Riba, D. Ponsa, and K. Mikolajczyk, “Key. net: Keypoint detection by handcrafted and learned cnn filters,” *Proceedings of the IEEE/CVF International Conference on Computer Vision*, pp. 5836–5844, 2019. **3**
- [28] X. Zhao, X. Wu, J. Miao, W. Chen, P. C. Chen, and Z. Li, “Alike: Accurate and lightweight keypoint detection and descriptor extraction,” *IEEE Transactions on Multimedia*, 2022. **3**

- [29] J. Zhang, D. Sun, Z. Luo, A. Yao, L. Zhou, T. Shen, Y. Chen, L. Quan, and H. Liao, "Learning two-view correspondences and geometry using order-aware network," *ICCV*, October 2019. **3**
- [30] W. Jiang, E. Trulls, J. Hosang, A. Tagliasacchi, and K. M. Yi, "Cotr: Correspondence transformer for matching across images," *Proceedings of the IEEE/CVF International Conference on Computer Vision*, pp. 6207–6217, 2021. **3**
- [31] X. Li, K. Han, S. Li, and V. Prisacariu, "Dual-resolution correspondence networks," *Advances in Neural Information Processing Systems*, vol. 33, pp. 17 346–17 357, 2020. **3**
- [32] D. Tan, J.-J. Liu, X. Chen, C. Chen, R. Zhang, Y. Shen, S. Ding, and R. Ji, "Eco-tr: Efficient correspondences finding via coarse-to-fine refinement," *European Conference on Computer Vision*, pp. 317–334, 2022. **3, 10**
- [33] I. Melekhov, A. Tiuipin, T. Sattler, M. Pollefeys, E. Rahtu, and J. Kannala, "Dgc-net: Dense geometric correspondence network," *2019 IEEE Winter Conference on Applications of Computer Vision (WACV)*, pp. 1034–1042, 2019. **3**
- [34] P. Truong, M. Danelljan, and R. Timofte, "Glu-net: Global-local universal network for dense flow and correspondences," *Proceedings of the IEEE/CVF conference on computer vision and pattern recognition*, pp. 6258–6268, 2020. **3**
- [35] K. Dai, T. Xie, K. Wang, Z. Jiang, R. Li, and L. Zhao, "Oamatcher: An overlapping areas-based network for accurate local feature matching," *arXiv preprint arXiv:2302.05846*, 2023. **3**
- [36] H. Song, Y. Kashiwaba, S. Wu, and C. Wang, "Efficient and accurate co-visible region localization with matching key-points crop (mkpc): A two-stage pipeline for enhancing image matching performance," 2023. **3, 13**
- [37] M. Dehghani, B. Mustafa, J. Djolonga, J. Heek, M. Minderer, M. Caron, A. Steiner, J. Puigcerver, R. Geirhos, I. Alabdulmohsin, A. Oliver, P. Padlewski, A. Gritsenko, M. Lučić, and N. Houlsby, "Patch n' pack: Navit, a vision transformer for any aspect ratio and resolution," 2024. **4, 10, 11, 19**
- [38] I. Balazevic, C. Allen, and T. Hospedales, "Multi-relational poincaré graph embeddings," *Advances in Neural Information Processing Systems*, vol. 32, 2019. **5**
- [39] V. Martínez, F. Berzal, and J.-C. Cubero, "A survey of link prediction in complex networks," *ACM Comput. Surv.*, vol. 49, no. 4, dec 2016. [Online]. Available: <https://doi.org/10.1145/3012704> **5**
- [40] P. Clifford, "Markov random fields in statistics," *Disorder in physical systems: A volume in honour of John M. Hammersley*, pp. 19–32, 1990. **6**
- [41] F.-Y. Wu, "The potts model," *Reviews of modern physics*, vol. 54, no. 1, p. 235, 1982. **6**
- [42] J. Yu, Y. Jiang, Z. Wang, Z. Cao, and T. Huang, "Unitbox: An advanced object detection network," in *Proceedings of the 24th ACM international conference on Multimedia*, 2016, pp. 516–520. **6**
- [43] Y. Boykov, O. Veksler, and R. Zabih, "Fast approximate energy minimization via graph cuts," *IEEE Transactions on Pattern Analysis and Machine Intelligence*, vol. 23, no. 11, pp. 1222–1239, 2001. **6**
- [44] Y. L. Junjie Ni, H. B. Zhaoyang Huang, Hongsheng Li, and G. Z. Zhaopeng Cui, "Pats: Patch area transportation with subdivision for local feature matching," *CVPR*, 2023. **6, 7, 10, 12, 15, 21**
- [45] L. Leal-Taixé, C. Canton-Ferrer, and K. Schindler, "Learning by tracking: Siamese cnn for robust target association," in *Proceedings of the IEEE conference on computer vision and pattern recognition workshops*, 2016, pp. 33–40. **6**
- [46] A. Vaswani, N. Shazeer, N. Parmar, J. Uszkoreit, L. Jones, A. N. Gomez, Ł. Kaiser, and I. Polosukhin, "Attention is all you need," *Advances in neural information processing systems*, vol. 30, 2017. **6**
- [47] C. M. Bishop and N. M. Nasrabadi, *Pattern recognition and machine learning*. Springer, 2006, vol. 4, no. 4. **6, 7, 8**
- [48] M. Tyszkiewicz, P. Fua, and E. Trulls, "Disk: Learning local features with policy gradient," *Advances in Neural Information Processing Systems*, vol. 33, pp. 14 254–14 265, 2020. **8**
- [49] A. Mao, M. Mohri, and Y. Zhong, "Cross-entropy loss functions: Theoretical analysis and applications," in *Proceedings of the 40th International Conference on Machine Learning*, ser. Proceedings of Machine Learning Research, A. Krause, E. Brunskill, K. Cho, B. Engelhardt, S. Sabato, and J. Scarlett, Eds., vol. 202. PMLR, 23–29 Jul 2023, pp. 23 803–23 828. **8**
- [50] A. Dai, A. X. Chang, M. Savva, M. Halber, T. Funkhouser, and M. Nießner, "Scannet: Richly-annotated 3d reconstructions of indoor scenes," *Proc. Computer Vision and Pattern Recognition (CVPR)*, *IEEE*, 2017. **8, 9, 13, 21**
- [51] Z. Li and N. Snavely, "Megadepth: Learning single-view depth prediction from internet photos," *Proceedings of the IEEE conference on computer vision and pattern recognition*, pp. 2041–2050, 2018. **8, 10**
- [52] I. Loshchilov and F. Hutter, "Decoupled weight decay regularization," *ICLR*, 2019. **8**
- [53] T. Schöps, T. Sattler, and M. Pollefeys, "BAD SLAM: Bundle adjusted direct RGB-D SLAM," in *Conference on Computer Vision and Pattern Recognition (CVPR)*, 2019. **10**
- [54] B. Thomee, D. A. Shamma, G. Friedland, B. Elizalde, K. Ni, D. Poland, D. Borth, and L.-J. Li, "Yfcc100m: the new data in multimedia research," *Commun. ACM*, vol. 59, no. 2, p. 64–73, jan 2016. [Online]. Available: <https://doi.org/10.1145/2812802> **10**
- [55] M. A. Fischler and R. C. Bolles, "Random sample consensus: a paradigm for model fitting with applications to image analysis and automated cartography," *Commun. ACM*, vol. 24, no. 6, p. 381–395, jun 1981. **11**
- [56] D. Barath, J. Noskova, M. Ivaschekin, and J. Matas, "Magsac++, a fast, reliable and accurate robust estimator," in *Proceedings of the IEEE/CVF Conference on Computer Vision and Pattern Recognition (CVPR)*, June 2020. **11**
- [57] J. Nam, G. Lee, S. Kim, H. Kim, H. Cho, S. Kim, and S. Kim, "Diffmatch: Diffusion model for dense matching," 2024. **12**
- [58] S. Li, Q. Zhao, and Z. Xia, "Sparse-to-local-dense matching for geometry-guided correspondence estimation," *IEEE Transactions on Image Processing*, vol. 32, pp. 3536–3551, 2023. **13**
- [59] X. Zou, J. Yang, H. Zhang, F. Li, L. Li, J. Gao, and Y. J. Lee, "Segment everything everywhere all at once," *Advances in neural information processing systems*, 2023. **15**
- [60] M. Syakur, B. Khotimah, E. Rochman, and B. D. Satoto, "Integration k-means clustering method and elbow method for identification of the best customer profile cluster," in *IOP conference series: materials science and engineering*, vol. 336. IOP Publishing, 2018, p. 012017. **19**



Yesheng Zhang (Student Member, IEEE) received the B.S. and M.S. degrees in biomedical engineering from Shanghai Jiao Tong University (SJTU), Shanghai, China, in 2016 and 2022. He is currently working toward the Ph.D. degree with the Department of Automation, School of Electronic Information and Electrical Engineering, SJTU. His research interests include feature matching, visual SLAM and 3D reconstruction.



Xu Zhao (Member, IEEE) received the Ph.D. degree in pattern recognition and intelligent system from Shanghai Jiao Tong University (SJTU), Shanghai, China, in 2011. He is currently a Full Professor with the Department of Automation, School of Electronic Information and Electrical Engineering, SJTU. He was a Visiting Scholar with the Beckman Institute, University of Illinois Urbana-Champaign, Urbana, IL, USA, from November 2007 to December 2008, and a Post-doc Research Fellow with Northeastern University, Boston, MA, USA, from August 2012 to August 2013. His research interests include visual analysis of human motion, machine learning and image/video processing.

TABLE 11

Experimental proof of resolution overfitting in Transformer-based methods. The experiments are conducted on ScanNet1500, measuring pose estimation accuracy. We select the training resolution 640×480 for PM, along with another resolution 896×672 which maintains the aspect ratio but increases the resolution.

Pose estimation AUC	$640 \times 480 (4/3)^\dagger$			$896 \times 672 (4/3)^\dagger$		
	AUC@5 \uparrow	AUC@10 \uparrow	AUC@20 \uparrow	AUC@5 \uparrow	AUC@10 \uparrow	AUC@20 \uparrow
LoFTR [11]	25.68	45.86	62.60	15.48	30.60	45.29
MESA+LoFTR	26.23 $+2.14\%$	46.06 $+0.44\%$	62.90 $+0.48\%$	18.17 $+17.37\%$	34.02 $+11.18\%$	49.13 $+8.48\%$
DMESA+LoFTR	24.37 -5.10%	44.42 -3.14%	61.34 -2.10%	17.58 $+13.57\%$	33.38 $+9.08\%$	48.35 $+6.76\%$
QT [21]	28.56	49.30	65.78	2.88	6.27	11.23
MESA+QT	28.74 $+0.63\%$	49.12 -0.37%	66.03 $+0.38\%$	5.53 $+92.01\%$	11.43 $+82.30\%$	18.62 $+65.81\%$
DMESA+QT	26.51 -7.18%	46.71 -5.25%	63.41 -3.60%	9.55 $+231.60\%$	20.20 $+221.17\%$	31.28 $+178.54\%$

† Input Resolution (Aspect Ratio).

**APPENDIX A
EXPERIMENTS OF RESOLUTION OVERFITTING ISSUE**

In this section, we provide the additional experiments to prove resolution overfitting issue in Transformer-based methods. Specially, we choose the famous LoFTR [11] and its improved variants QT [21] as the baselines. In ScanNet, their training size is 640×480 with the aspect ratio $4/3$. Intuitively, the resolution overfitting is highly related to the aspect ratio, as which leads to the distortion of image context. Thus, we conduct comparison experiments on another size 896×672 , which maintains the same aspect ratio and improves the resolution. Considering the larger resolution brings more details and no distortion with the same aspect ratio, the performance between two sizes should be comparable. However, as we reported in Tab. 11, the performance of the baselines showcase significant descend (28.56 vs. 2.88 for QT on AUC@5). This proves the severe resolution overfitting issue of Transformer-based point matchers, which is possibly caused by the positional embedding [37]. On the other hand, our methods can increase the performance of the point matchers at the resolution of 896×672 (31.28 of DMESA+QT vs. 11.23 of QT). Nevertheless, although we set the area image size as the training resolution of 640×480 , our methods bring limited improvement (MESA) or even decrease the performance (DMESA). This can be attributed to **1**) the area images we cropped from the original images possess the original aspect ratio ($1296/968 = 486/363$) (cf. Sec. 3.3), which is slightly different from the training one ($640/480 = 484/363$); **2**) the excessive area size adjustment hinders the matching redundancy reduction achieved by our methods.

**APPENDIX B
BENEFITS OF A2PM**

In this section, we provide more detailed description about the benefit of the A2PM framework. See Fig. 11. The A2PM framework leverage the AM to split the original matching task into multiple easier inside-area matching tasks. Due to the reduced matching redundancy, area pair images contain substantial local details benefiting PM, which can be omitted by the original PM during resize operation. Another benefit comes from the cropping operation of A2PM, which can get the PM input with required resolution while maintaining the aspect ratio inherent to the raw image. Conversely, the resize operation widely applied in PM can result in severe distortion due to the aspect ratio variation (see the “resized input” in the Fig. 11). However, the premise of the above advantages is accurate area matching, which is the pursuit of the proposed MESA and DMESA.

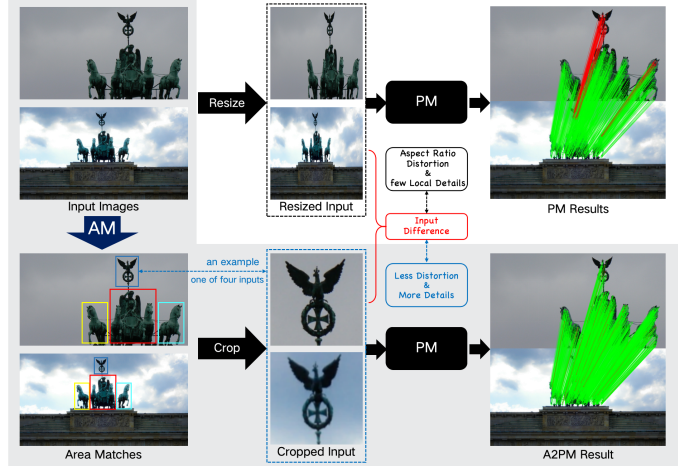


Fig. 11. **The benefit of the A2PM framework.** Essentially, the A2PM framework changes the input of PM. Based on the accurate AM, the matching redundancy is reduced, thus facilitating the inside-area PM with sufficient local details. Also, the cropping operation can avoid distortion from aspect ratio modification, which can be severe in resize operation (top).

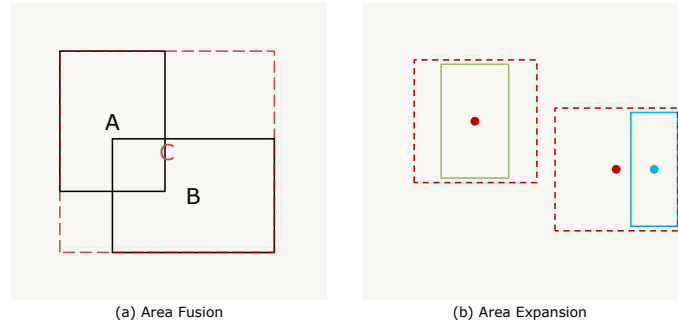


Fig. 12. **The Area Fusion and Area Expansion.** (a) Area fusion is to achieve the smallest area (C) containing the input areas (A and B). (b) Generally, area expansion is to fix the original area center and expand its size to the smallest size of the next level. When the original area is too close to the image boundary, we will move the area center to keep the expanded area inside the image.

**APPENDIX C
DETAILS OF AG COMPLETION**

In this section, we provide additional details of completing the Area Graph (AG). The initial AG contains few directed edges, due to the splitting nature of SAM, which hinders robust and efficient matching. Thus, we propose to generate more graph nodes to form a tree structure for AG, i.e. the graph completion algorithm. The detailed process for the graph completion is depicted in Algorithm 1, which takes initial AG (\mathcal{G}_{ini}) as input and outputs the final AG (\mathcal{G}) with scale hierarchy. Furthermore, we describe the area clustering and two main area operations adopted to generate higher level nodes in the algorithm as follows.

C.1 Area Clustering.

For orphan nodes in each level, we cluster them based on their area centers to decide which operation will be performed on them. We use the k-means algorithm with elbow method [60] to determine the cluster number. The candidate cluster number is set as $\{1, \dots, n\}$, where n is the number of orphan nodes in the current level. This algorithm is fed with area centers and outputs labeled ones.

Algorithm 1: Graph Completion

Input: $\mathcal{G}_{ini} = \langle \mathcal{V}_{ini}, \mathcal{E}_{ini} \rangle$
Output: $\mathcal{G} = \langle \mathcal{V}, \mathcal{E} \rangle$

```

1 for  $l$  in  $[0, L - 1]$  do
2   initial orphan node set  $\mathcal{O} = \emptyset$ ;
3   for  $v_i \in \{v_i | l_{a_i} = l\}$  do
4     if  $v_i$  has no parent then
5       add  $v_i$  into  $\mathcal{O}$ ;
6   cluster the nodes in  $\mathcal{O}$  based on their area centers;
7   for each node cluster  $\mathcal{C}_h = \{v_k\}_{k=0}^C$  do
8     if  $C \geq 2$  then
9       for each  $v_k \in \mathcal{C}_h$  do
10        if  $v_k$  has not been fused then
11          fuse area  $a_k$  with its nearest neighbor
12             $a^n | v^n \in \mathcal{C}_h: a^f = F(a_k, a^n)$ ;
13          generate higher level node  $v^f$  for
14             $a^f$ ;
15          add  $v^f$  into  $\mathcal{V}_{ini}$ ;
16          form edges by Link Prediction:
17             $\{e_h\}_h = LP(v^f, \mathcal{V}_{ini})$ ;
18          add  $\{e_h\}_h$  into  $\mathcal{E}_{ini}$ ;
9       else
10        Update the single node  $v_0: v_0^u = Up(v_0)$ ;
11        construct edges:  $\{e_j\}_j = LP(v_0^u, \mathcal{V}_{ini})$ ;
12        add  $\{e_j\}_j$  into  $\mathcal{E}_{ini}$ ;
20  $\mathcal{E} = \mathcal{E}_{ini}$ ;
21  $\mathcal{V} = \mathcal{V}_{ini}$ ;
22 output the updated AG:  $\mathcal{G} = \langle \mathcal{V}, \mathcal{E} \rangle$ ;

```

C.2 Area Fusion and Expansion.

Area fusion and expansion are key operations in our graph completion algorithm. Specifically, area fusion is to find the largest outer rectangle of the two areas as the new area, as depicted in Fig. 12 (a). Due to the careful threshold settings of our area level, the fused area size will exceed current level and be awaited for subsequent operations. On the other hand, the expansion operation is to expand the area to the next level size (Fig. 12 (b)). In particular, suppose the lower bound of size for the next level is s^2 , if both of the area width and height are smaller than s , we expand the height and width of the area to s , keeping the area center fixed. Otherwise if area width $w \geq s$, we let the area height $h = s^2/w$, keeping the area center fixed, and vice versa. The above operations are performed when the expanded area is inside the image. On the other hand, if the expanded area is outside the image, the area center will be moved as shown in Fig. 12 (b).

APPENDIX D

COMPUTATION COMPLEXITY ANALYZE OF MESA

Here, we analyze the computation complexity of proposed graphical area matching, demonstrating the main source of the efficiency issue in MESA.

D.1 Area Similarity Calculation

Firstly, area similarity calculation is performed to achieve the required node energies in the graph, serving as the prerequisite of our graphical area matching. Suppose we have two AGs, \mathcal{G}^0

and \mathcal{G}^1 , for the input image pair, \mathcal{G}^0 gets N nodes ($|\mathcal{V}^0| = N$) and \mathcal{G}^1 gets M nodes ($|\mathcal{V}^1| = M$). Therefore, the dense graph energy calculation needs $M \times N$ times similarity calculation. However, owing to the similarity conditional independence of ABN (Sec. 4.2.3), the actual number ($M' \times N'$) of similarity calculation is smaller than $M \times N$, as $N' < N$. Nevertheless, directly setting children pair similarities as 0 is too rough (Eq. (11)), as large scale differences also leads to near-zero similarity between areas. In practise, we only set the related similarities of *next level children* as 0 for area matching accuracy and the efficiency from ABN is still helpful to our approach. Moreover, we only care about the similarities between source nodes in \mathcal{G}^0 and other nodes in \mathcal{G}^1 , because we collect source nodes with specific level from \mathcal{G}^0 to match, e.g., usually 3 ~ 4 areas in indoor scene and less in outdoor scene. Therefore, we have $M' < M$. Similarly, in the case of duality, i.e., collecting source nodes from \mathcal{G}^1 to match, we only need to perform a few supplementary calculations, as similarities are symmetric and reusable. Thus, the real computation complexity of area similarity computation is $O(M' \times N')$, where $M' \times N' < M \times N$.

D.2 Edge Energy Calculation

Except the node energy calculation, the edge energy is also needed to be determined for *Graph Cut*. The computation complexity of edge energy calculation is related to edge number of \mathcal{G}^0 and \mathcal{G}^1 . Assume $|\mathcal{E}_0| = E$ and $|\mathcal{E}_1| = K$, the specific computation complexity is $O(E + K)$.

D.3 Global Energy Minimization

In our global energy minimization for area matching refinement, the matching energy of parent, children and neighbour pairs all need to be calculated. Taking parent matching energy for example, we derive its computation complexity as follows. Suppose n nodes are achieved as match candidates through *Graph Cut* and each node gets Q_i , $i \in (0, n]$ parent nodes, there are $Q_i \times V$ node similarities need to be accessed (as the similarity calculation is finished), where V is the parent node number of the source node. Hence, the total computation complexity for parent matching energy in global energy minimization is $O(\sum_i^n Q_i \times V)$. The children matching energy and neighbour matching energy are similar. As n is the number of node after *Graph Cut*, it is small in most cases, e.g., usually < 3 area nodes. Moreover, the number of parent nodes (or children, neighbour nodes) is also limited. Therefore, the computation complexity for global energy minimization is acceptable in practise.

In sum, the efficiency issue of MESA mainly lies in the Area Similarity Calculation part, which contains quadratic computational complexity. This issue comes from the sparse area matching framework in MESA, thus motivating us to design the dense counterpart, DMESA.

APPENDIX E

ADDITIONAL ABLATION STUDY

E.1 Ablation Study on Image Cropping

The image cropping is a trivial yet important operation in the A2PM framework, as different cropping approaches lead to different image quality and distortions. Here, we construct experiments to investigate the impact of different cropping approaches. To be specific, we compare two different cropping methods: 1) the

TABLE 12

Ablation study of area image cropping. Two different image cropping methods are compared for the proposed MESA. Both semi-dense and dense point matchers are combined for evaluation. We report the pose estimation $AUC@5^\circ/10^\circ/20^\circ$ and the **best** results of two series are highlighted respectively.

Method	Cropping Approach	AUC@5 \uparrow	AUC@10 \uparrow	AUC@20 \uparrow
MESA+ASpan	$C \rightarrow R$	24.67	43.72	61.29
	$E \rightarrow C$	27.51	47.47	65.04
MESA+DKM	$C \rightarrow R$	30.19	51.49	68.79
	$E \rightarrow C$	33.42	55.04	71.98

TABLE 13

Ablation study of global energy parameters. We compare different parameter settings for global energy refinement in MESA_ASpan and report the area matching performance, area number per image (AreaNum), and the pose estimation performance. Results are highlighted as **first**, **second** and **third**.

E_G Parameters	$T_{E_{max}}$	AOR \uparrow	AMP@0.6 \uparrow	Pose AUC@5° \uparrow	AreaNum \uparrow
$\mu = 5, \alpha = 2,$ $\beta = 2, \gamma = 1$	0.35	61.76	65.54	23.57	4.69
	0.25	63.91	71.13	22.41	3.47
	0.15	60.44	62.57	21.46	3.27
$\mu = 4, \alpha = 2,$ $\beta = 2, \gamma = 2$	0.35	67.98	80.09	23.74	5.76
	0.25	64.94	72.24	24.01	4.62
	0.15	61.74	65.50	23.55	3.86
$\mu = 7, \alpha = 1,$ $\beta = 1, \gamma = 1$	0.35	65.98	78.10	22.71	3.27
	0.25	62.32	66.54	23.56	2.92
	0.15	60.32	64.38	22.37	2.77

straightforward cropping method ($C \rightarrow R$), which **cropps** areas with original aspect ratios and then **resizes** them to input resolution; **2)** the $E \rightarrow C$ cropping method, which first **expands** the area to correspond with the aspect ratio of the point matcher input and then **cropps** these areas. The experiment is conducted on ScanNet1500 [50] benchmark. We combine MESA with both semi-dense (ASpan) and dense (DKM) point matchers for complete comparison. Results are summarized in Tab. 12. As we can see that the $E \rightarrow C$ cropping approach outperforms the $C \rightarrow R$ approach with a large margin for both MESA+ASpan and MESA+DKM, proving its superiority due to high resolution and less distortion. Therefore, we adopt the $E \rightarrow C$ approach for area image cropping.

E.2 Ablation Study on Global Energy Parameters

The parameters for our global energy refinement in MESA mainly consists of global energy balance parameters (E_G Parameters) in Eq. (12) and the threshold parameter $T_{E_{max}}$. The four E_G Parameters reflect the importance of four energy terms, *i.e.*, self matching energy, parent, children and neighbour matching energy. The $T_{E_{max}}$ controls the maximum energy of the final match, the smaller it is the stricter the refinement. Here, we construct experiments on ScanNet1500 to investigate the performance impact of these parameters. In particular, we compare three groups of E_G Parameters and three groups of $T_{E_{max}}$ to evaluate their impact on MESA_ASpan. The input size of ASpan is 480×480 . The area matching performance, pose estimation performance and area number per image are summarised in Tab. 13. Generally, if two areas are matched, their parent, children and neighbour nodes should have high similarities due to spatial relationships between them. At the same time, the self matching energy should still be an important reference in matching refinement. Thus we choose three parameter settings including different weights on three kinds of node matching energies and different emphasis on self-matching energy. The experiment results in Tab. 13 show that the weights of

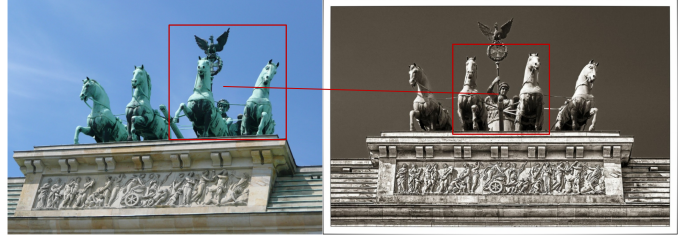


Fig. 13. **The Failure case on MegaDepth of MESA.** MESA may produce false area matches when repeated objects and viewpoint variance occur at the same time. The impact of this kind of erroneous match can be alleviated by post-processing like GAM [18].

three parameter settings set to the same is better for area matching performance ($\alpha = \beta = \gamma$ *vs.* $\alpha = \beta \neq \gamma$). Giving sufficient consideration on global matching leads to accurate area matching along with best point matching performance ($\mu = 4$ *vs.* $\mu = 7$). Despite the semi-dense matcher is not sensitive to area matching accuracy, better area matching leads to higher pose estimation precision. Therefore, we choose [4, 2, 2, 2] as our energy setting. On the other, the $T_{E_{max}}$ is a critical parameter as well. The smaller $T_{E_{max}}$ means stricter global matching energy request, but it may also mistake some accurate area matches when too small. Different E_G Parameter settings prefer different values of $T_{E_{max}}$ and 0.35 suits the best for ours.

APPENDIX F

LIMITATION AND FUTURE WORK

One common limitation of MESA and DMESA is the under-utilisation of SAM features. As we mentioned before, SAM possesses the high-level image understanding across a wide range of domains due to the massive training dataset and carefully designed models. Therefore, its image embedding is a extremely strong high-level representation, which has the potential to replace our learning similarity model. Then, the computation cost can be reduced as well. However, the naive attempt to use SAM features as descriptors of areas failed, possibly because the SAM segmentation pays more attention on intra-image contexts rather than inter-image ones like feature matching. Hence, the SAM feature needs further distillation for area matching, which will be an objective of our future work.

On the other hand, as MESA fuses image areas based on their 2D distances, which may not be lifted equivalently to 3D. Thus, some inconsistent area fusions between two images arise and lead to inaccurate point matching, *e.g.*, shown in Fig. 13. Although the post-processing like GAM [18] may help, it also introduces extra computation cost. To address this issue, feature-guided fusion can be adopted, where the SAM feature can be employed and lead to consistent area fusion.

Finally, there is a optimization space related to efficiency for the A2PM framework. Although the area matching speed of DMESA aligns with the current SOTA, the overall matching process of the A2PM framework is still time-intensive. This can be attributed to that the original *single* matching task is divided into multiple matching tasks by A2PM. This issue can be addressed by parallel computation and GPU acceleration like PATS [44]. On the other hand, considering the significant precision improvement achieved by our methods, they are valuable for some downstream tasks that are not sensitive to time cost, such as SfM.